




Article

Rare Earth Element Phases in Bauxite Residue

Johannes Vind ^{1,2,*} , Annelies Malfliet ³, Bart Blanpain ³, Petros E. Tsakiridis ² ,
Alan H. Tkaczyk ⁴ , Vicky Vassiliadou ¹ and Dimitrios Panias ²

¹ Department of Continuous Improvement and Systems Management, Aluminium of Greece Plant, Metallurgy Business Unit, Mytilineos S.A., Agios Nikolaos, 32003 Boeotia, Greece; vicky.vassiliadou@alhellas.gr

² School of Mining and Metallurgical Engineering, National Technical University of Athens, Iroon Polytechniou 9, Zografou Campus, 15780 Athens, Greece; ptsakiri@central.ntua.gr (P.E.T.); panias@metal.ntua.gr (D.P.)

³ Department of Materials Engineering, KU Leuven, Kasteelpark Arenberg 44, P.O. Box 2450, B-3001 Leuven, Belgium; annelies.malfliet@kuleuven.be (A.M.); bart.blanpain@kuleuven.be (B.B.)

⁴ Institute of Physics, University of Tartu, Ostwaldi 1, 50411 Tartu, Estonia; alan@ut.ee

* Correspondence: johannes.vind@alhellas.gr; Tel.: +30-210-7722184

Received: 30 January 2018; Accepted: 15 February 2018; Published: 24 February 2018

Abstract: The purpose of present work was to provide mineralogical insight into the rare earth element (REE) phases in bauxite residue to improve REE recovering technologies. Experimental work was performed by electron probe microanalysis with energy dispersive as well as wavelength dispersive spectroscopy and transmission electron microscopy. REEs are found as discrete mineral particles in bauxite residue. Their sizes range from $<1\ \mu\text{m}$ to about $40\ \mu\text{m}$. In bauxite residue, the most abundant REE bearing phases are light REE (LREE) ferrotitanates that form a solid solution between the phases with major compositions $(\text{REE}, \text{Ca}, \text{Na})(\text{Ti}, \text{Fe})\text{O}_3$ and $(\text{Ca}, \text{Na})(\text{Ti}, \text{Fe})\text{O}_3$. These are secondary phases formed during the Bayer process by an in-situ transformation of the precursor bauxite LREE phases. Compared to natural systems, the indicated solid solution resembles loparite-perovskite series. LREE particles often have a calcium ferrotitanate shell surrounding them that probably hinders their solubility. Minor amount of LREE carbonate and phosphate minerals as well as manganese-associated LREE phases are also present in bauxite residue. Heavy REEs occur in the same form as in bauxites, namely as yttrium phosphates. These results show that the Bayer process has an impact on the initial REE mineralogy contained in bauxite. Bauxite residue as well as selected bauxites are potentially good sources of REEs.

Keywords: bauxite; bauxite residue; red mud; rare earth elements; rare earth minerals; rare earth ferrotitanate; perovskite; loparite

1. Introduction

It can be argued that humankind is mostly heading on a collision path with the ecosystems of the Earth [1]. One of the sectors bearing responsibility for the damaging actions is the minerals industry. For instance, the world's largest rare earth element (REE) mine Bayan Obo has a large footprint which can have a major ecological impact while providing the largest proportion of worldwide REE supplies [2]. The future of critical metals industry as well as any other industry must increasingly follow the practices of concepts in responsible sourcing [3].

REEs are defined as lanthanides, found in the periodic table from atomic numbers 57–71, with the first one of them being lanthanum. Due to the chemical similarities, yttrium is also categorised as a REE. The REEs are typically subdivided into light REEs (LREE) and heavy REEs (HREE). The LREEs are elements from lanthanum to europium, HREEs are yttrium and gadolinium to lutetium, although this division is ambiguous [4]. Scandium is not considered as part of the REEs group in the present

work, though it is also often defined as an REE. The reason for omitting scandium is that (1) in geochemical systems, scandium does not behave similarly to the lanthanides [5], and (2) scandium has been shown to occur in contrasting forms compared to the lanthanides in bauxite and bauxite residue [6]. REEs have numerous applications and are often considered as the backbone of high-tech and green technology [4].

Bauxite residue (or filtered red mud) is a by-product of alumina refining from bauxite ore. It poses problems for the alumina industry due to the huge volume of the residue accumulated (2.7 billion tonnes) [7] and volume produced (150 million tonnes) each year worldwide [8]. The primary potentially dangerous property of bauxite residue is its alkalinity, that can have an adverse impact when the residue is not handled safely [8,9]. Upon the release of bauxite residue to the environment, as happened in 2010 in Ajka (Hungary), threats of ecotoxicity can arise from the presence and release of metals and metalloids such as vanadium, chromium and molybdenum to the environment. Bauxite residue has a very fine particle size and fugitive dust from this material can influence the health of residents in nearby areas, while this effect is considered equal or lower than for similar dusts in densely populated areas [9]. The efforts of remediating bauxite residue disposal sites as well as developing processes that attempt to utilise bauxite residue as a raw material are ongoing [7–11].

Bauxite residue has been recognised for possible additional advantages in responsible REE sourcing compared to, for example, REE-bearing carbonatite rocks. The qualitatively identified advantages include the fact of being a by-product as well as low radioactivity levels [3]. When considering a ten-year perspective of REE demand in context of the potential advantages of the deposit types, bauxite residue in addition to the ion adsorption clay deposits have been deemed to offer good opportunities for the production of REEs [12].

Defining new resources of critical metals like the REEs is obviously also important from an economic point of view. European Commission lists REEs as critical raw materials. This classification is based on two main criteria, economic importance and supply risk [13]. Another characteristic issue of the REEs economy and market is the REEs balance problem. Although there is a high demand for some specific REEs (e.g., neodymium), others (e.g., cerium) are oversupplied due to their higher abundance in the ores. This imbalance is also reflected in the prices of individual REEs [14]. Again, bauxite residue has been proposed as a possible relief for the supply risk as well as the balance problem of the REEs [10,14,15].

Most of the present work is performed on a qualitative basis because of the diverse nature of REE species found in bauxite residue. However, quantification is taken into practice for elucidating the characteristics of the most frequently encountered REE mineral types. Raman spectroscopy was trialled as a complementary microanalytical tool to aid the specific identification of carbonate species, which would be difficult to define unambiguously by the electron microprobe analysis. This approach has shown good results in identifying REE minerals in bauxite [16].

The aim of this work is to reveal the types of REE phases contained in bauxite residue. The newly gained knowledge will contribute to the development of REE extraction technologies from bauxite residue. Existing knowledge is briefly reviewed in Sections 2–5 to provide the state of the art in the discussed matters.

2. Bauxite, Parnassos-Ghiona Deposit

Bauxite is a type of alumina-rich rock, which is formed during the weathering of various kinds of aluminosilicate source rocks [17]. A major division is made between lateritic bauxite deposits (88% of the world's resources) and karst bauxite deposits (12% of world's resources) [18]. The former types of deposits are situated immediately on the source rocks as weathered crusts. The prevailing alumina mineral is gibbsite, in the form of aluminium hydroxide [17]. Karst bauxite deposits are associated with carbonate rocks, where bauxite bodies fill former karst cavities. Commonly, the source material of karst bauxite originates from a neighbouring area and has been transported during the formation of the deposit. The main alumina minerals in karst bauxite are diasporite and boehmite, in forms of

aluminium oxyhydroxides. Due to the high content of alumina in bauxite, it is the main industrial ore source to obtain technically pure alumina and aluminium [19].

The Parnassos-Ghiona bauxite deposit is situated in Central Greece, north of the Gulf of Corinth. It is a karst type of deposit, associated by its genesis with other deposits in the Mediterranean region. Bauxite ore bodies form layers or irregular bodies that are intercalated between the Mesozoic limestones. The principal minerals found in the deposit are boehmite, diaspore and hematite [19,20]. The deposit is sub-divided into three bauxite horizons. The upper horizon (B3) is currently being industrially exploited [21] and the middle horizon (B2) exploited to a limited extent as far as we know.

3. REEs Geochemistry and Phases in Bauxite

REEs are relatively more enriched in karst bauxite deposits compared to lateritic deposits [17]. In the bauxite profiles, REEs concentration increases towards the lower sections and is the highest immediately near the footwall limestone [22]. Concentrations may differ by four magnitudes between the upper and lower parts of the profiles [23]. In some instances, total REEs concentration near the carbonate footwall can reach a remarkable 1 wt % [23,24]. In such cases, REE minerals can even be identified by XRD analysis [25]. This pattern is explained by the partial dissolution of REEs into the percolating pore fluids in the bauxite profile. Then, REEs are precipitated as secondary (authigenic) minerals near the carbonate footwall, where the fluids encounter an alkaline pH barrier. The migration is noted for both LREEs and HREEs [22]. However, some fractionation in the REEs group is also noted. Namely, cerium is sometimes more concentrated in the upper sections of the profile. Cerium can occur in a tetravalent state in oxidative conditions. It precipitates as cerianite, $(\text{Ce}^{4+}, \text{Th})\text{O}_2$, in the upper parts of some bauxite profiles, while other cerium species like the fluorocarbonates are more often found in lower sections of the profiles [22,26].

First efforts to elucidate the characteristics of REE mineral species in bauxites were taken up in the 1970s [27]. It was revealed that REEs can be found as detrital minerals, i.e., minerals in the same form as they occur in the parent rocks of bauxites. In this category, mainly phosphate phases like monazite $((\text{Ce}, \text{La}, \text{Nd}, \text{Th})\text{PO}_4)$ and xenotime (YPO_4) have been identified [27,28]. In bauxites, REEs also occur as authigenic phases, i.e., phases that have been precipitated in situ within the bauxite profile from percolating fluids. Such phases are commonly REE fluorocarbonates of the bastnäsite $(\text{Ce}(\text{CO}_3)\text{F})$ mineral group or phosphates of monazite group [25,29]. Often, occurrences of hydroxylbastnäsite are reported, in which fluorine ion is substituted with hydroxyl ion $(\text{REE}(\text{CO}_3)(\text{OH}))$ [22,24,29]. Moreover, hydroxylbastnäsite has been highlighted as the most frequently identified REE mineral in karst bauxites [29]. Raman spectroscopy was successfully applied to aid the identification of authigenic monazite-Nd and authigenic xenotime in Zagrad karst bauxite deposit (Montenegro) [16]. Cerium can occur in the oxide form as authigenic cerianite [26]. Some occurrences of REEs in bauxites are also attributed to the ion adsorption form on clay or diaspore surfaces [30]. It has also been reported that REE mineral composition can be highly variable even in bauxite samples collected a few meters apart from each other [25]. This list of REE minerals in bauxites is not exhaustive as there is a wide variety of REE phases described. An increasing volume of research is being published about the mineralogy of REEs in bauxite deposits worldwide in the recent years [16,30–32]. An overview and a case study of the REEs geochemistry in European bauxite deposits as well as in the derived residues is given by Dedy et al. [15]. As can be seen from the preceding reviews, REE minerals found in bauxite deposits are often like the ones that are commonly exploited in the existing REE mines, namely monazite, bastnäsite and xenotime [33].

4. Bayer Process and Bauxite Residue Relating to the REEs

Alumina is worldwide almost exclusively produced by the Bayer process, patented in 1888 by Karl Josef Bayer [8,34–37]. It utilises sodium hydroxide pressurised digestion to dissolve the aluminium (oxy-)hydroxide minerals and discards the remaining mineral matrix. From the digestion effluent slurry after leaching, solid fraction is separated as bauxite residue by settling and washing. The current

practise in Aluminium of Greece plant (Metallurgy Business Unit, Mytilineos S.A.; hereafter denoted as AoG) is to apply filter pressing and then dry-stacking the bauxite residue [8]. Aluminium hydroxide is precipitated from the pregnant leach liquor and spent liquor is routed back to the beginning of the process, while spent liquor is concentrated in the evaporation unit before a new cycle. Alumina (Al_2O_3) is produced in the calcination unit from aluminium hydroxide [7,38].

Details of the processing conditions differ between the refineries, but the digestion temperatures usually vary from 100 to 260 °C [7,39]. AoG uses about 80% of Greek karstic bauxite and 20% of lateritic bauxite (from Ghana or Brazil) in their process feed. Digestion of the karstic bauxite slurry is performed at about 255 °C at a pressure of about 3.5 MPa [40], meaning this is a high temperature process by the terminology of alumina industry [7]. The need to use high temperature is dictated by the mineralogical nature of karst bauxite, where the hard to dissolve boehmite and diasporite prevail as the alumina phases [7]. Retention time of the slurry in the digestion autoclaves is about one hour. Lateritic bauxite slurry is introduced to the main karstic bauxite slurry in the appropriate flash stage after the high temperature digestion of karst bauxite slurry. This method is known as the “sweetening process” where monohydrate and trihydrate bauxites are used simultaneously and thus the productivity of the plant is increased [41].

During the Bayer process, the bulk of REEs is almost entirely transferred to bauxite residue, based on case studies of lanthanum, scandium [42], cerium and yttrium distribution in the Bayer process [43].

Depending on the concentration of REEs in the bauxite ore, bauxite residue can have a concentration of total REEs up to 2500 mg/kg such as in the case of the example of Jamaican bauxite residue [44]. In AoG’s bauxite residue, total REEs concentration ranges from 800 to 1100 mg/kg [15,45]. During a 15-year period, the REEs concentration in AoG’s bauxite residue has fluctuated only about 8% [46]. The noteworthy REE concentrations are commonly associated with bauxite residue derived from karstic bauxite [11,47].

So far, the REE occurrence modes and phases in bauxite residue have not been unambiguously explained [11]. Several authors have expressed the difficulties of speciating the REE phases [48,49]. Regardless of the scarcity of information, some observations can be summarised. Doubtful identifications of allanite and dissakite have been reported from a XRD diffractogram of an Indian bauxite residue sample. With only about 110 mg/kg concentration of cerium in the sample [50], it is not realistic that REE mineral phases result in XRD reflections. The authors also reported from EPMA analysis, that dispersed REEs presence was correlated with aluminium- and silicate-rich areas rather than with iron-rich areas of the sample [50]. In a patent describing the recovery of REEs from bauxite residue, REEs have been indicated to occur in calcium titanate phases that were created in the Bayer process. According to the source, they correspond mineralogically to perovskite [51]. It was noted that in a Greek bauxite residue sample (from AoG), cerium presence might be related to the occurrence of a loparite type phase (belonging to perovskite group). The suggestion was based on a STEM-EDS investigation, where the presence of thorium and possibly some trace amount of cerium were identified in a mineralogically proven perovskite form ($\text{Ca}_{0.8}\text{Na}_{0.2}\text{TiO}_3$) [52]. In a Canadian bauxite residue sample (Jonquière, Québec), REE-containing particles were noted as bright spots in electron backscatter imaging, sub- μm in size. A STEM-EDS elemental mapping also showed the presence of REE-containing particles, where cerium and titanium presence were correlated [53]. Based on the observations of bauxite residue leaching behaviour, Bayer process secondary minerals like cancrinite and hydrogarnet have also been proposed as the possible hosts of REEs [54]. Hematite has been proven to be able to incorporate tetravalent cerium into its lattice. Based on that and the existence of cerium in hematite-enriched matrix of bauxite residue, hematite was suggested to contain cerium in its lattice as the potentially prevailing form of cerium occurrence in bauxite residue [55]. In the same study, the heavy minerals fraction was found to contain some sporadic grains of bastnäsite and monazite, but they were considered as negligible carriers of REEs. Cerium was identified to occur in its tetravalent oxidation state in the bulk sample and therefore the common REE minerals (e.g., monazite) were excluded as the potential hosts of cerium [55]. The authors admitted that cerium location in

hematite lattice remains hypothetical, but they insist that REEs occurrence in bauxite residue should be discussed in the context of main mineral phases rather than discrete REE phases [55].

Summaries about the recovery of REEs from bauxite residue can be found from different publications [10,11,46,56]. In general, the methods follow a hydrometallurgical route or a combination of pyro- and hydrometallurgical routes. Recently developed technologies have successfully applied ionic liquid leaching on bauxite residue to selectively recover REEs from bauxite residue [46].

5. Materials and Methods

The materials analysed in this work are from the AoG plant. AoG is located in Central Greece, Boeotia. Three samples were investigated: (1) karst bauxite from Greece (Parnassos-Ghiona deposit, B3 horizon), (2) lateritic bauxite from Ghana (Awaso deposit), and (3) dewatered bauxite residue. All samples were collected in year 2016 from AoG. Bauxite samples were studied to expand existing knowledge about the precursor REE phases entering to the Bayer process. Main attention of the investigation was given for bauxite residue sample.

The proportion of samples subjected to bulk characterisation was crushed and ground, dried at 100 °C overnight and split according to standard techniques. The parts of samples subjected to microscale investigation were embedded in resin, polished and coated with carbon (qualitative investigations) or platinum (quantitative investigations). Bauxite residue “as is” was attached to sample holder and coated with gold for secondary electron imaging. Bauxite residue subsample (~0.5 g) that was analysed in nanoscale, was suspended in acetone and treated with ultrasound to disaggregate the coagulated particles. The sample was then placed on a 300-mesh carbon coated copper grid and air-dried overnight.

Bulk chemical composition of the main oxides was determined by XRF (Perform'X, Thermo Fisher Scientific™, Waltham, MA, USA) by the fused glass bead method [57]. Trace element concentrations were measured by inductively coupled plasma mass spectrometry (ICP-MS, Xseries 2, Thermo Fisher Scientific™, Waltham, MA, USA) after lithium metaborate/tetraborate fusion or by instrumental neutron activation analysis (INAA, Activation Laboratories Ltd., Ancaster, ON, Canada). The quality of trace element analysis was assessed by analysing standard bauxite reference material BX-N for both methods (ICP-MS and INAA). In the case of ICP-MS, higher than suggested deviations were detected in lanthanum, praseodymium, dysprosium and erbium concentrations, and the rest of the element concentrations were within acceptable limits. Mineralogical composition was determined by X-ray diffraction (XRD, Bruker, Billerica, MA, USA) with Bruker D8 Focus. Identification of mineral phases was performed with XDB Powder Diffraction Phase Analytical System version 3.107 that is specifically designed for analysing bauxite and bauxite residue [58,59].

Qualitative microscale investigations were performed by electron probe microanalysis (EPMA) with energy dispersive spectroscopy (EDS,) with (1) EVO MA15 (ZEISS, Oberkochen, Germany) coupled with AZtec X-MAX 80 (Oxford Instruments, Abingdon, UK), and (2) JEOL 6380 LV (JEOL, Tokyo, Japan). EMPA-EDS instruments were operated at 20 kV. Microscale quantitative analyses were performed with a field emission microprobe JEOL JXA-8530F (JEOL, Tokyo, Japan) coupled with wavelength dispersive spectrometers (WDS): (1) TAP/LDE1, (2) LIF/PET, (3) LDE2H/TAPH, (4) LIFH/PETH, (5) LIFH/PETH. It was operated at 15 kV with a probe current of 30 nA. The standards used are listed in Table 1. Nanoscale investigation of bauxite residue was performed with a high resolution JEOL JEM-2100 LaB6 transmission electron microscope (HRTEM) (JEOL, Tokyo, Japan), operating at 200 kV. Grain microstructure was also studied using a bright field detector in scanning (STEM) mode of JEM-2100 instrument. Elemental analyses were carried out using an Oxford X-Max 100 Silicon Drift Energy Dispersive X-ray spectrometer (Oxford Instruments, Abingdon, UK), connected to TEM, with a probe size ranging from 2 to 5 nm in STEM mode.

Table 1. Standards used for wavelength dispersive spectroscopy (WDS) quantification.

No.	Element	Standard Name	Formula
1	Na	Albite	Na(AlSi ₃ O ₈)
2	Al	Albite	
3	Si	Diopside	CaMgSi ₂ O ₆
4	Ca	Diopside	
5	Fe	Hematite	Fe ₂ O ₃
6	La	Monazite	(Ce,La,Nd,Th)PO ₄
7	Ce	Monazite	
8	Th	Monazite	
9	Nd	Neodymium glass	SiO ₂ -CaO-Al ₂ O ₃ -Nd ₂ O ₃
10	Mg	Periclase	MgO
11	Pr	Praseodymium glass	SiO ₂ -CaO-Al ₂ O ₃ -Pr ₂ O ₃
12	Ti	Rutile	TiO ₂

Microscale in-situ Raman spectroscopy was performed using Renishaw inVia confocal Raman microscope (Renishaw, Wotton-under-Edge, UK), operated with a 532-nm laser. Raman spectra were processed with Spectragryph 1.0.7 software. For presenting purposes, some EDS spectra were smoothed with Spectragryph 1.0.7 [60]. Retrieved Raman spectra were compared with reference data from RRUFF database [61].

6. Results and Discussion

6.1. Bulk Characterisation

Both bauxite samples have aluminium oxide as a major component, followed by iron oxide while minor amounts of silicon and titanium oxide are also present (Table 2). Calcium oxide is present in the Greek karstic bauxite sample and not in the Ghanaian lateritic bauxite. As a contrast to bauxite samples, bauxite residue's main component is iron oxide, but there is also present an appreciable amount of unrecovered aluminium oxide. The high amount of calcium oxide is mainly attributed to lime addition in the Bayer process. Sodium oxide content appears from the losses of sodium hydroxide that binds with secondary minerals created during bauxite processing, due to transformation of clay minerals to desilication products and reaction of quartz resulting in the same [62].

Greek karst bauxite sample is composed mainly of diaspore, boehmite, hematite, goethite, anatase, calcite and kaolinite. Ghanaian lateritic bauxite sample is composed mainly of gibbsite, hematite, goethite, kaolinite and rutile. Primary mineral phases, those that are already present in bauxite, detected in bauxite residue are hematite, diaspore, boehmite and goethite. Secondary mineral phases, that were formed in the Bayer process, are hydrogarnet, cancrinite, perovskite and gibbsite. Obviously, the content of REEs in the studied samples (Table 3) is too low to be able to detect any REE mineral phases by XRD.

Higher REEs concentration between the two bauxite samples is found to be in the Greek karst bauxite (Table 3). The most abundant REE in all samples is cerium (Ce). The resulting bauxite residue has about two times higher REE concentration compared to bauxite feed.

Table 2. Major oxide composition of the samples.

Oxide	Karst Bauxite Greece	Lateritic Bauxite Ghana	Bauxite Residue Greece, AoG
	wt %	wt %	wt %
LOI	11.3	29.7	9.2
Al ₂ O ₃	58.3	55.9	20.2
Fe ₂ O ₃	21.0	11.0	44.6
SiO ₂	2.5	1.2	5.3
TiO ₂	2.7	1.6	5.7
CaO	1.7	<0.01	9.1
Na ₂ O	0.4	0.09	2.3
MnO	0.02	0.02	0.04
Total	97.9	99.4	96.4

Table 3. Trace element composition of the samples. Error is given as one standard deviation of a duplicate measurement.

Element	Karst Bauxite Greece	Lateritic Bauxite Ghana	Bauxite Residue Greece, AoG
	ICP-MS	INAA	ICP-MS
	(mg/kg)	(mg/kg)	(mg/kg)
La	57 ± 7	19.1 ± 1.3	130 ± 1
Ce	206 ± 8	34 ± 1	480 ± 26
Pr	15 ± 1	n/a	29 ± 2
Nd	53 ± 6	13 ± 1	107 ± 0
Sm	9.8 ± 1.0	2.0 ± 0.2	19.4 ± 0.2
Eu	2.4 ± 0.9	0.8 ± 0.2	4.6 ± 1.1
Gd	10.6 ± 0.6	n/a	22.0 ± 0.3
Tb	2.3 ± 0.5	<0.5	3.3 ± 0.0
Dy	9.8 ± 0.3	n/a	20.1 ± 0.1
Ho	2.1 ± 0.1	n/a	4.1 ± 0.1
Er	7.2 ± 0.8	n/a	13.3 ± 0.3
Tm	<2	n/a	<2
Yb	7.0 ± 0.4	2.5 ± 0.3	13.8 ± 0.3
Lu	<2	0.4 ± 0.0	2.2 ± 0.0
Y	48 ± 2	n/a	108 ± 2
Nb	55 ± 9	n/a	100 ± 1
Th	51 ± 2	22.7 ± 2.3	105 ± 2
ΣLn ¹	382.3		854.4
ΣREE ²	430.6		962.5

¹ Sum of lanthanides; ² Sum of lanthanides and yttrium.

6.2. Precursor REE Phases in AoG's Bauxite Feed

In Table 4 are shown the REE phases that are likely to be introduced to AoG's production line via the composition of bauxite feed. In Parnassos-Ghiona bauxite profiles (Prossorema and Frussia), detrital rhabdophane and florencite have been identified as LREE phases, whereas detrital churchite and xenotime represent HREE phases [28]. Hydroxylbastnäsite-(La) and -(Nd) were identified in the lowermost bauxite profile samples of Parnassos-Ghiona deposit (Mandri Tsakni) as the only contribution that deployed WDS quantification [24]. Authigenic bastnäsite and parisite group phases were further reported as representatives of authigenic fluorocarbonate LREE minerals in Parnassos-Ghiona bauxite (Pera Lakkos) [63]. As it is not clear on what basis was the distinction of parisite group from the rest of calcium-bearing REE phases made, we categorise it together with other calcium containing LREE fluorocarbonates, synchysite and röntgenite [64]. A recent report questions the earlier identifications of cerium-predominant REE phases, that they could be rather

cerium oxides or carbonates, because of the absence of phosphorus and fluorine. Due to the absence of other lanthanides, even the identification as hydroxylbastnäsite-Ce is being questioned [65].

Table 4. Precursor REE phases in the bauxite feed of AoG refinery.

Phase	Formula	Parnassos-Ghiona Karst				Ghana Lateritic
		[24]	[28]	[63,66]	[65]	Present
LREE						
rhabdophane-(Ce)	(Ce)(PO ₄)·H ₂ O		+			
florencite-(Ce)	CeAl ₃ (PO ₄) ₂ (OH) ₆		+	+		+
bastnäsite group	Ce(CO ₃)F			+		
parisite/synchysite/röntgenite	Ca ₁₋₂ REE ₁₋₃ (CO ₃) ₂₋₅ F ₁₋₃			+		+
hydroxylbastnäsite-(Nd) and -(La)		+				
cerianite	CeO ₂				?	+
HREE						
churchite	YPO ₄ ·2H ₂ O		+			
xenotime	YPO ₄		+			+

In the studied Parnassos-Ghiona bauxite samples, some areas are particularly rich in REE phases (Figure 1). Authigenic cerium-predominant LREE phases in sizes over 10 µm are concentrated into iron and aluminium oxide matrix rather than to alumina-rich pisolithic textures. This is in line with the observations made by Mongelli [26], where he noted that cerium is more fractionated to the bauxite matrix as opposed to ooids (pisoliths). However, the ooids described by Mongelli [26] are controlled by hematite matrix which is different from present observation. This textural fractionation has not been reported in the case of Parnassos-Ghiona bauxite deposit. The LREE phases were identified by µ-Raman spectroscopy being cerianite (CeO₂), following the main band at 457 cm⁻¹, when comparing with the reference spectrum R050379 from RRUFF database and those spectra given in the literature sources (Figure 1b) [61,67]. Based on the analysis of synthetic and natural cerianite specimens, this band can be attributed to the symmetric breathing mode of Ce–O–Ce bond [67,68]. The band at 396 cm⁻¹ present on the reference spectrum R050379, but missing in current experimental spectrum, is rarely noted in different cerianite Raman spectra [67,68]. The band at 396 cm⁻¹ could also be hidden due to the broadening of 457 cm⁻¹ band. Broadening as well as shifting of cerianite main band is noted to occur along with decreasing particle size [69]. Notably, the acquired spectrum lacks the presence of Raman bands that could be associated with the occurrence of carbonate (around 1100 cm⁻¹) or hydroxide ions (3400–3600 cm⁻¹) [67,70]. The matrix where cerianite is situated, is mainly controlled by hematite, following the Raman bands at 225, 293 and 409 cm⁻¹ [61,71]. Zaitsev et al. have demonstrated that fluorine can also be present in cerianite [67]. Fluorine is also present in cerianite of Parnassos-Ghiona bauxite (Figure 1a). Some of the previously reported REE phases might have been erroneously identified as bastnäsite group phases on qualitative basis when judged only by the presence of fluorine. Thus, current results support the doubts of Mouchos et al. regarding the cerium-predominant phases [65] and evidence is provided for the identification of cerianite in Parnassos-Ghiona bauxite.

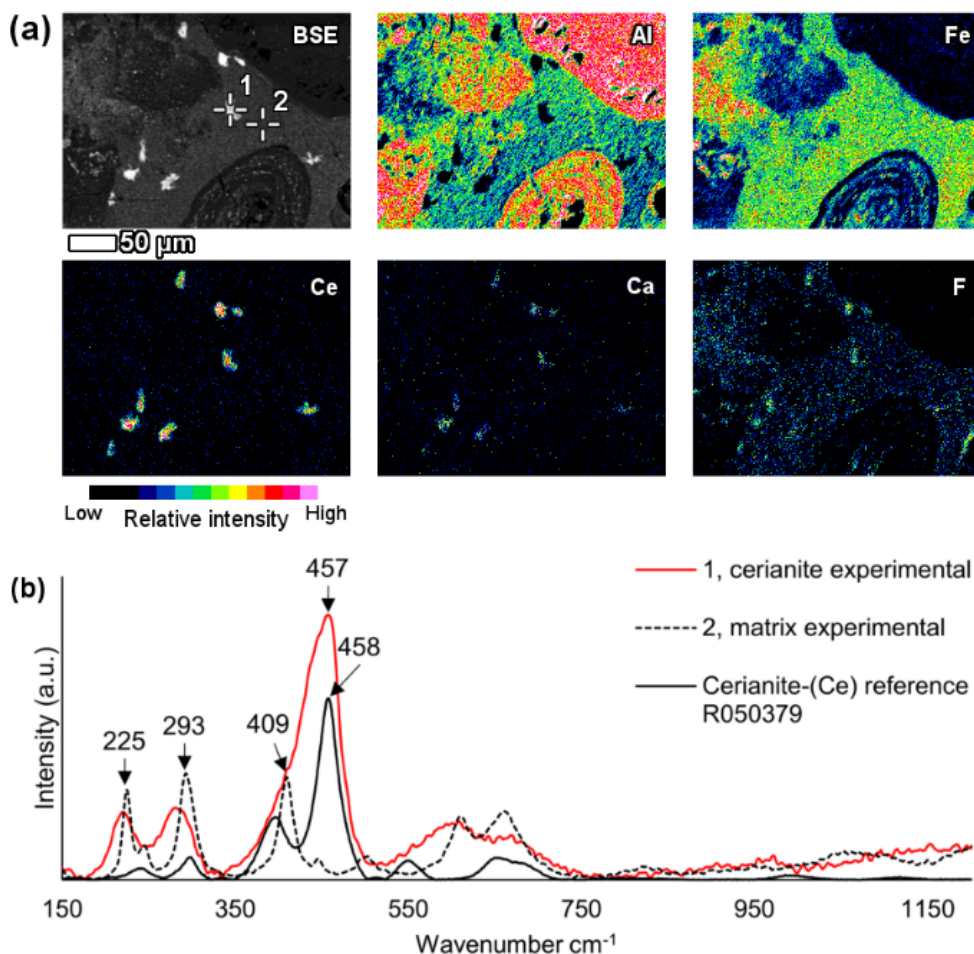


Figure 1. Cerianite rich area in Parnassos-Ghiona bauxite shown on (a) backscattered electron (BSE) image with respective EDS elemental maps, and (b) Raman spectra of cerianite and its surrounding matrix compared to reference Raman spectrum obtained from RRUFF database [61], with permission from RRUFF™. Raman spectrum collected with a 532-nm wavelength laser.

Authigenic cerium-predominant REE phases were noted to be associated with fissures filled with aluminosilicate matrix that is likely kaolinite (Figure 2). Kaolinite-associated authigenic REE phases have not been reported before, but their presence has been assumed in Parnassos-Ghiona bauxite due to the easily leachable proportion of REEs [72]. It was noted previously, however, that some detrital florencite crystals were encased within clay fragments [28].

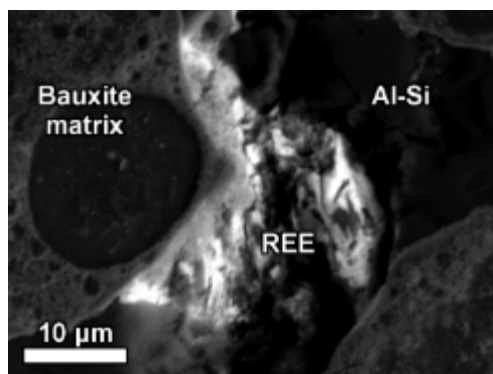


Figure 2. REE phase in Parnassos-Ghiona bauxite associated with aluminosilicate (Al-Si).

Regardless of the low REEs concentration in Ghanaian bauxite (Table 3), distinct detrital REE phases are also contained within this lateritic bauxite (Figure 3). The REE minerals have a prevailing content of aluminium, followed by cerium, phosphorus and then other LREEs. Thus, these REE phases can be identified as belonging to the florencite group. In addition, detrital xenotime was identified in the Ghanaian bauxite. Florencite grains are significantly larger (20–50 μm) than xenotime grains (1–3 μm). The presence of florencite and xenotime group phases in Ghanaian lateritic bauxite implies granitic origin of the bauxite parent material.

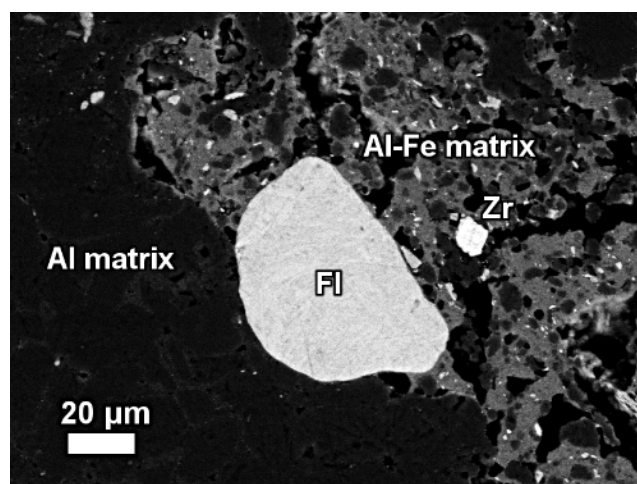


Figure 3. Florencite group LREE phase (Fl) and a zircon grain (Zr) in Ghanaian lateritic bauxite matrix.

The main input of LREE phases introduced to the Bayer process in AoG along with the bauxite feed therefore appear to be LREE fluorocarbonates of the bastnäsite group as well as cerianite. Minor LREE input is from phosphate phases. Heavy REEs enter the process as phosphate-based groups. Elucidating the REE mineralogy in the Parnassos-Ghiona bauxite deposit deserves a thorough investigation in terms of clearly defining the mineral phases and their spatial distribution along the bauxite profile. The currently existing information is scattered and not uniform.

6.3. REE Phases in Bauxite Residue

In bauxite residue, REE mineral particles appear in the backscattered electron imaging mode as bright particles. They are contrasting in their brightness from other bauxite residue phases like hematite, diaspore/boehmite, hydrogarnet, titanium dioxides, cancrinite or perovskite (Figure 4). The formerly mentioned phases (hematite, diaspore/boehmite, hydrogarnet, titanium dioxides, cancrinite, perovskite) are distinguishable from each other in EPMA analysis. At a similar brightness level as the REE particles, other heavy mineral particles such as for instance, zircon, chromite, pyrite and chalcopyrite were revealed. Even metallic iron chips with the presence of chromium are present. The latter are thought to originate from the grinding equipment of the alumina refining plant.

6.3.1. REE Carbonate and Phosphate Phases

In the investigated bauxite residue sample, a neodymium and lanthanum predominant particle with the presence of carbon was revealed (Figure 5). Other LREEs like praseodymium and gadolinium were also present. The particle was notably large, more than 40 μm in its longest dimension and exhibited a blocky crystal habit.

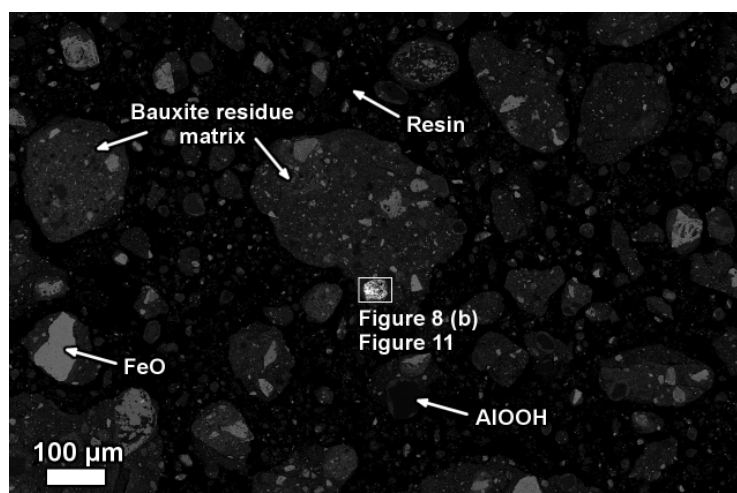


Figure 4. Backscattered electron image of bauxite residue. The bright REE particle in the middle corresponds to the particle depicted on Figures 8(b) and 11.

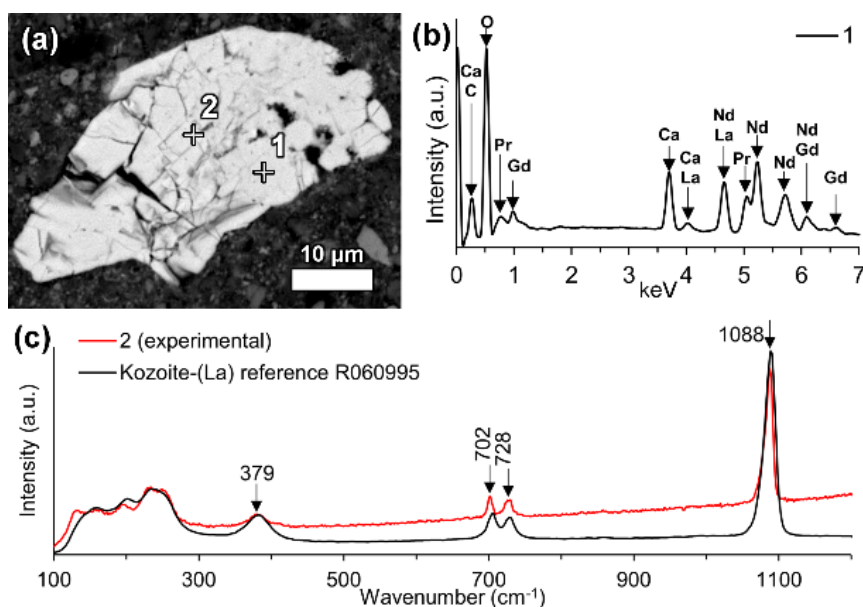


Figure 5. An ancylite group LREE carbonate phase depicted on (a) backscattered electron image with its (b) EDS spectrum and (c) Raman spectrum compared to a reference spectrum of kozoite-(La) obtained from RRUFF database [61], with permission from RRUFF™. Raman spectrum collected with a 532-nm wavelength laser.

Raman investigation of this grain resulted in a spectrogram showing a major peak at 1088 cm^{-1} , that can be attributed to symmetric C–O stretching of CO_3^{2-} (Figure 5c) [73,74]. Comparison with reference data from RRUFF database resulted in a notably similar match with the kozoite-(La) ($\text{La}(\text{CO}_3)(\text{OH})$) Raman spectrum [61]. The observed peak at 1088 cm^{-1} is the most characteristic one for the ancylite group phases [61,73]. Kozoite, belonging to the ancylite mineral group, is dimorphous with hydroxylbastnäsite. In other words, it has identical chemical composition, but different mineral structure. The former occurs in orthorhombic crystal system and the latter in hexagonal [75]. The kozoite-(La) reference spectrum given in the RRUFF database has not yet been confirmed by other identification methods. Therefore, the present identification cannot be regarded as conclusive. However, the absence of other matching spectra and the relative similarity with other ancylite group minerals Raman spectra [61] allows at least suggesting that the investigated particle belongs to ancylite

mineral group. Other LREE particles in bauxite residue analysed with Raman spectroscopy did not result in unambiguously interpretable Raman spectra, did not provide any Raman scattering bands or were overwhelmed with fluorescence.

The formerly described evidence shows that a part of LREEs can occur as carbonate phases in bauxite residue. Ancylyte group minerals have not been identified in any bauxite sample. It could be that they have been reported as hydroxylbastnäsite species because of their identical chemical composition. Generally, REE carbonate phases are expected to be dissolved during sodium hydroxide digestion [33]. Based on the above-mentioned evidence, it is difficult to define whether the LREE carbonate phase is a primary mineral inherited from bauxite that withstood Bayer digestion conditions or is a secondary precipitate form created in the Bayer process. In any case, it is a very rare occurrence type in bauxite residue.

In a few cases, LREEs are found as calcium containing phosphate phases in bauxite residue, more specifically as cerium phosphates. It can be seen from the EDS spectrum of an analysed particle, exhibiting a pronounced phosphorus X-ray peak (Figure 6). This and other similar observed grains are cerium predominant. The low amount of LREE phosphate species in bauxite residue is in line with the relative scarcity of phosphate phases in the AoG's bauxite feed. The composition of these grains resembles rhabdophane-Ce that has been detected in Parnassos-Ghiona bauxite [28]. It is an indication that REE phosphates endure, at least partly, the Bayer process. This is an expected behaviour as REE phosphates do not dissolve easily in sodium hydroxide, although there are processes that apply sodium hydroxide leaching to recover REEs from phosphate minerals like monazite and xenotime [32]. In such processes, sodium hydroxide is more concentrated (40–50% NaOH) [33] than in the Bayer process (12–22% NaOH) [39].

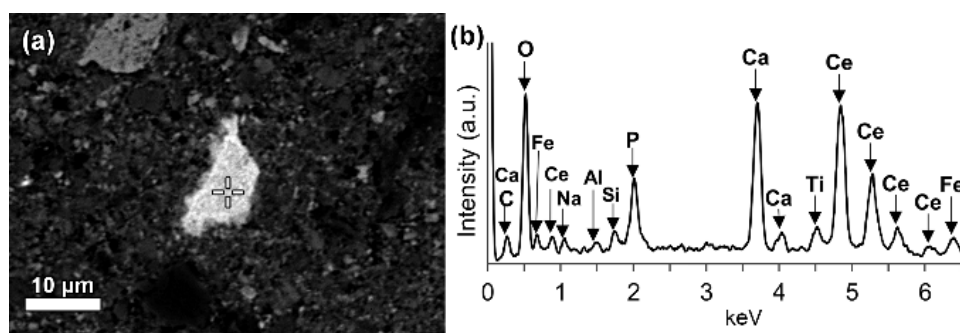


Figure 6. Cerium phosphate in bauxite residue matrix, shown on (a) backscattered electron image with its (b) EDS spectrum.

6.3.2. LREE Ferrotitanate Species, $(\text{REE,Ca,Na})(\text{Ti,Fe})\text{O}_3$

In bauxite residue, LREE mineral particles that contain calcium, titanium, iron and sodium (Figures 7 and 8, Tables 5 and 6) are also found. They further divide into cerium predominant (Table 5) and neodymium-lanthanum predominant particles (Table 6). The number of ions in the mineral formula shown in Tables 5 and 6 have been calculated based on a perovskite stoichiometry with three oxygen atoms (ABO_3). Alternatively, the number of ions could be calculated by adopting the double perovskite structure with the composition $\text{A}_2\text{B}_2\text{O}_6$ [76]. Division of the ions between A and B sites is based on previous literature, considering their charges and relative ionic radii [76,77]. The chemical composition of these particles is variable, for instance Ce_2O_3 content ranges from about 34 to 51 wt % while TiO_2 content ranges from 9 to 24 wt % (Table 5). It can be noted that measurements 1–6 in Table 6 are relatively depleted in Fe_2O_3 content, although the title of this section refers to ferrotitanate species. This effect is explained further in the text below. Such chemical composition which is uncommon for REE phases in bauxite, especially the appreciable presence of sodium, clearly indicates that the LREE ferrotitanates are formed during the Bayer process.

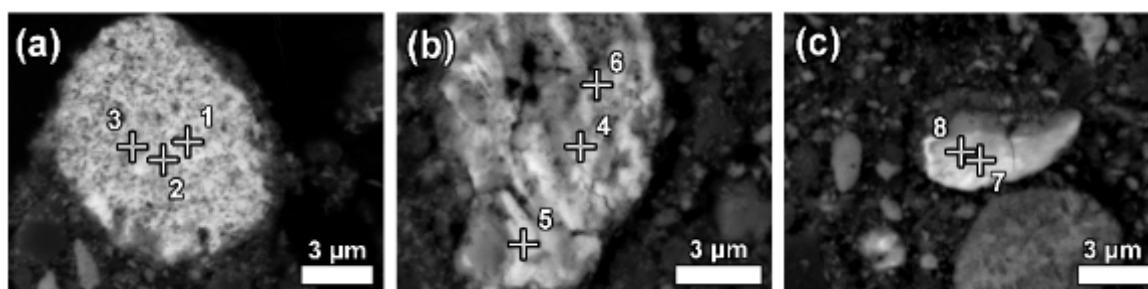


Figure 7. Backscattered electron images of cerium ferrotitanate grains in bauxite residue matrix (a–c). The indicated quantification spots are reported in Table 5.

Table 5. EPMA-WDS quantification (wt %) of cerium predominant ferrotitanate grains (Figure 7). Lower section of the table shows the number of ions in the mineral formula, following the ABO_3 perovskite structure.

Oxide	Figure 7 Quantification							
No.	1	2	3	4	5	6	7	8
La ₂ O ₃	1.65	1.21	1.31	0.09	0.10	0.11	1.28	1.10
Ce ₂ O ₃	51.25	45.36	48.13	47.22	44.67	34.48	45.52	47.27
Pr ₂ O ₃	1.30	0.82	0.86	0.00	0.10	0.07	1.31	1.24
Nd ₂ O ₃	2.48	1.93	2.00	1.41	1.54	1.00	3.30	2.99
TiO ₂	9.00	9.16	9.44	14.84	21.78	18.56	21.37	23.86
Fe ₂ O ₃	17.85	22.33	21.98	14.84	8.77	22.87	7.80	7.32
CaO	4.34	4.01	4.13	6.56	8.78	9.91	7.93	9.59
MgO	0.02	0.05	0.03	0.01	0.02	0.22	0.03	0.01
SiO ₂	0.98	0.97	0.98	1.00	1.21	2.09	1.53	1.59
Na ₂ O	0.90	1.32	0.92	0.92	1.49	2.16	2.01	3.21
Al ₂ O ₃	1.39	1.43	1.30	1.13	1.12	2.01	1.50	1.39
ThO ₂	2.68	1.99	2.21	1.36	1.36	1.21	0.02	0.02
Total	93.83	90.58	93.28	89.36	90.94	94.70	93.60	99.58
No. of ions per ABO_3 formula								
La	0.03	0.02	0.02	0.00	0.00	0.00	0.02	0.01
Ce	0.81	0.73	0.75	0.71	0.61	0.44	0.61	0.58
Pr	0.02	0.01	0.01	0.00	0.00	0.00	0.02	0.02
Nd	0.04	0.03	0.03	0.02	0.02	0.01	0.04	0.04
Ti	0.29	0.30	0.30	0.46	0.61	0.49	0.58	0.60
Fe	0.58	0.73	0.71	0.46	0.25	0.60	0.21	0.18
Ca	0.20	0.19	0.19	0.29	0.35	0.37	0.31	0.35
Mg	0.00	0.00	0.00	0.00	0.00	0.01	0.00	0.00
Si	0.04	0.04	0.04	0.04	0.05	0.07	0.06	0.05
Na	0.08	0.11	0.08	0.07	0.11	0.15	0.14	0.21
Al	0.07	0.07	0.07	0.06	0.05	0.08	0.06	0.06
Th	0.03	0.02	0.02	0.01	0.01	0.01	0.00	0.00
Structural formulas following the ABO_3 structure								
A (REE, Ca, Na, Th)	1.20	1.11	1.11	1.11	1.10	0.99	1.14	1.20
B (Ti, Fe, Al, Si)	0.99	1.15	1.12	1.02	0.95	1.24	0.92	0.90

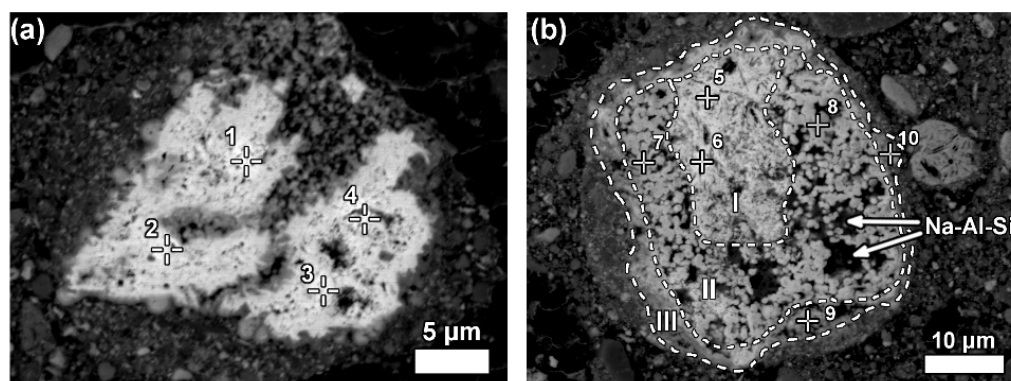


Figure 8. Neodymium-lanthanum predominant LREE particles, of which (a) is partly reacted, and (b) exhibits a zonation (I–III) relating to reaction stages with Bayer liquor. Within zone II of (b), deposition of a sodium aluminosilicate phase (Na–Al–Si) is indicated.

Table 6. EPMA-WDS quantification (wt %) of a neodymium-lanthanum predominant partly reacted LREE grain (1–4) (Figure 8a) and a LREE ferrotitanate grain (5–10) (Figure 8b). Lower section of the table shows the number of ions in the mineral formula, following the ABO_3 perovskite structure.

Oxide	Figure 8 Quantification									
No.	1	2	3	4	5	6	7	8	9	10
La ₂ O ₃	23.21	24.93	25.99	25.49	23.89	23.89	10.25	13.87	1.06	7.41
Ce ₂ O ₃	7.87	8.87	10.57	10.47	5.99	5.46	2.71	3.49	0.58	1.29
Pr ₂ O ₃	21.91	20.56	20.79	21.90	22.02	20.78	9.41	8.45	1.03	5.60
Nd ₂ O ₃	35.10	33.73	33.59	34.02	34.92	34.19	14.37	17.22	1.71	8.53
TiO ₂	3.87	5.85	0.83	3.08	1.44	2.03	27.48	24.13	32.60	40.35
Fe ₂ O ₃	2.61	2.35	2.20	3.27	6.67	4.07	10.71	12.21	42.44	12.26
CaO	2.11	3.07	1.93	2.56	1.46	1.12	4.42	5.64	17.92	14.16
MgO	0.00	0.00	0.01	0.00	0.11	0.08	0.99	0.02	0.03	0.03
SiO ₂	0.16	0.29	0.17	0.20	0.38	0.54	2.93	1.25	1.57	2.30
Na ₂ O	0.16	0.62	0.00	0.14	0.00	0.00	5.65	4.46	2.87	6.93
Al ₂ O ₃	0.28	0.34	0.33	0.25	0.66	0.88	3.21	1.36	1.07	2.13
ThO ₂	0.00	0.00	0.00	0.00	0.09	0.07	0.05	0.02	0.01	0.04
Total	97.28	100.62	96.40	101.37	97.62	93.11	92.17	92.12	102.89	101.02
No. of atoms per ABO_3 formula										
La	0.44	0.43	0.52	0.46	0.45	0.47	0.12	0.18	0.01	0.07
Ce	0.15	0.15	0.21	0.19	0.11	0.11	0.03	0.05	0.01	0.01
Pr	0.41	0.35	0.41	0.39	0.41	0.41	0.11	0.11	0.01	0.05
Nd	0.64	0.57	0.65	0.60	0.64	0.65	0.17	0.22	0.02	0.08
Ti	0.15	0.21	0.03	0.11	0.06	0.08	0.67	0.65	0.67	0.81
Fe	0.10	0.08	0.09	0.13	0.26	0.16	0.26	0.33	0.87	0.25
Ca	0.12	0.16	0.11	0.13	0.08	0.06	0.15	0.22	0.52	0.40
Mg	0.00	0.00	0.00	0.00	0.01	0.01	0.05	0.00	0.00	0.00
Si	0.01	0.01	0.01	0.01	0.02	0.03	0.09	0.04	0.04	0.06
Na	0.02	0.06	0.00	0.01	0.00	0.00	0.35	0.31	0.15	0.36
Al	0.02	0.02	0.02	0.01	0.04	0.06	0.12	0.06	0.03	0.07
Th	0.00	0.00	0.00	0.00	0.00	0.00	0.00	0.00	0.00	0.00
Structural formulas following the ABO_3 structure										
A (REE, Ca, Na)	1.76	1.72	1.90	1.79	1.72	1.71	0.99	1.08	0.72	0.98
B (Ti, Fe, Al, Si)	0.27	0.32	0.15	0.27	0.37	0.33	1.15	1.08	1.61	1.18

Some LREE particles were observed that have a relatively small percentage of iron, titanium and sodium oxide content (Figure 8a, Table 6). Others showed distinct zonation expressed in wide variation in chemical composition as well as in morphological features (Figure 8b, Table 6).

The texture of LREE ferrotitanate grains is anhedral. Secondary electron imaging of bauxite residue “as is” revealed that LREE ferrotitanate grains are partly covered with submicron-sized bauxite residue matrix particulate (Figure 9). At most, aggregates of anhedral globular crystallites can be observed when examining larger particles that exhibit different reaction stages. This can be seen in Figure 8b, especially in the zone II.

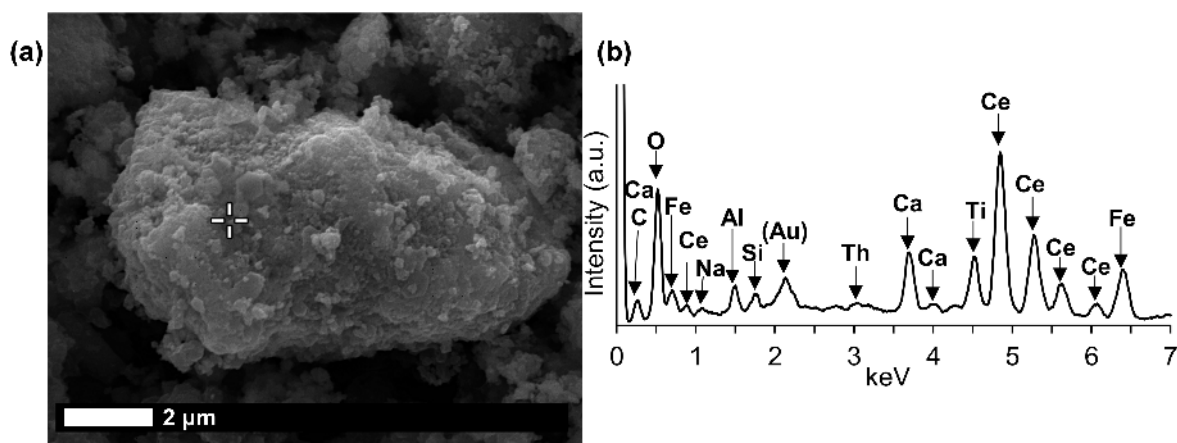


Figure 9. Cerium ferrotitanate particle shown on (a) secondary electron image with its (b) EDS spectrum; gold (Au) peak is from the coating layer on the sample.

In addition, LREE-containing globular calcium ferrotitanate particles were discerned in nanoscale investigation with HRTEM (Figure 10, Appendix A Table A1). The maximum concentrations of REEs measured in EDS were about 3 wt % of cerium and about 2.5 wt % of lanthanum (Table A1). The quantities of REEs below 1 wt % were regarded as unreliable due to the poor ability of EDS to measure trace constituents. Selected area electron diffraction (SAED) of a LREE bearing particle resulted in a reflection pattern indicating to a well crystallised character. The *d*-values (*d* = 0.2564 nm) measured from the patterns resemble the ones of conventional perovskite reference (*d* = 0.2710 nm) from [121] direction. Most of the calcium ferrotitanate particles were, however, REE-depleted. Other REE-containing phases were not confidently discerned among the fine particulates of bauxite residue during nanoscale HRTEM investigation.

From the previously noted observations, an important conclusion should be made. Calcium ferrotitanate species, likely corresponding mineralogically to perovskite, with low LREE concentration, should not be confused with the REE-barren perovskite *sensu stricto* (CaTiO_3) that is also found in bauxite residue, as detected in XRD diffractograms. Such perovskite is created by a different reaction route. Namely, titanium dioxide phases, especially anatase, react partially with sodium hydroxide and then with lime added to Bayer process and as a result form perovskite *sensu stricto* [78].

When the LREE ferrotitanate particles are relatively large (20–30 μm), the variations in their chemical composition can be drawn out by elemental mapping (Figure 11). It is seen in Figure 11, that the highest REEs concentrations are found in the core of the particle. REE concentration decreases towards the edges of the particle. In the bauxite residue matrix surrounding the particle, there are no presence of REEs. The trend is the opposite for titanium, calcium and sodium. Their concentration increases towards the edges of the particle. While the change in titanium concentration is quite gradual from core to edge, there is a more sudden increase of calcium concentration on the rim of the particle. The gradual change of the chemical composition refers to the existence of a solid solution between the LREE predominant and calcium predominant end-members. Another characteristic feature of the reacted LREE ferrotitanate particles is that the outer layer tends to form a distinct calcium ferrotitanate shell around the particle, where LREEs concentrations are low (Ti, Ca and Fe maps on Figure 11). The zone that contains about an equal amount of titanium and REEs (corresponding to

zone II on Figure 8b, or silica rich area in Figure 11, indicated with Na-Al-Si), is also intergrown with a sodium aluminium silicate phase. This likely corresponds to a secondary Bayer process phase, sodalite or cancrinite.

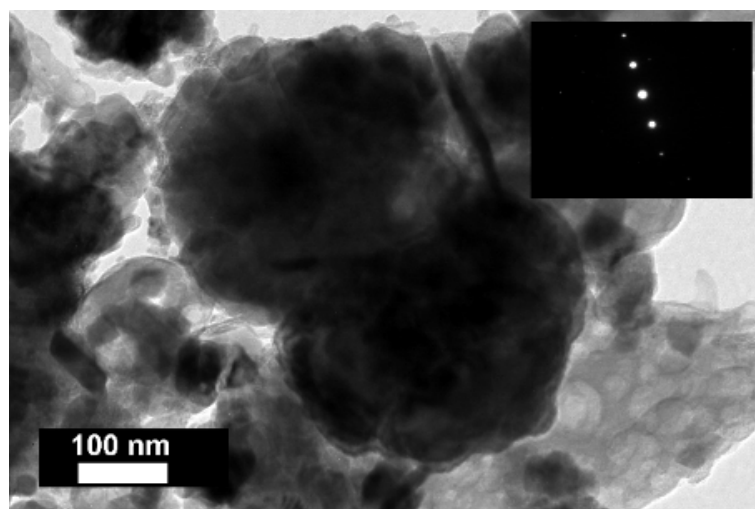


Figure 10. LREE-bearing titanium ferrotitanate observed in the bright field imaging mode of HRTEM. SAED pattern of the particle is inserted to the upper right corner. The pattern is collected from [121] direction.

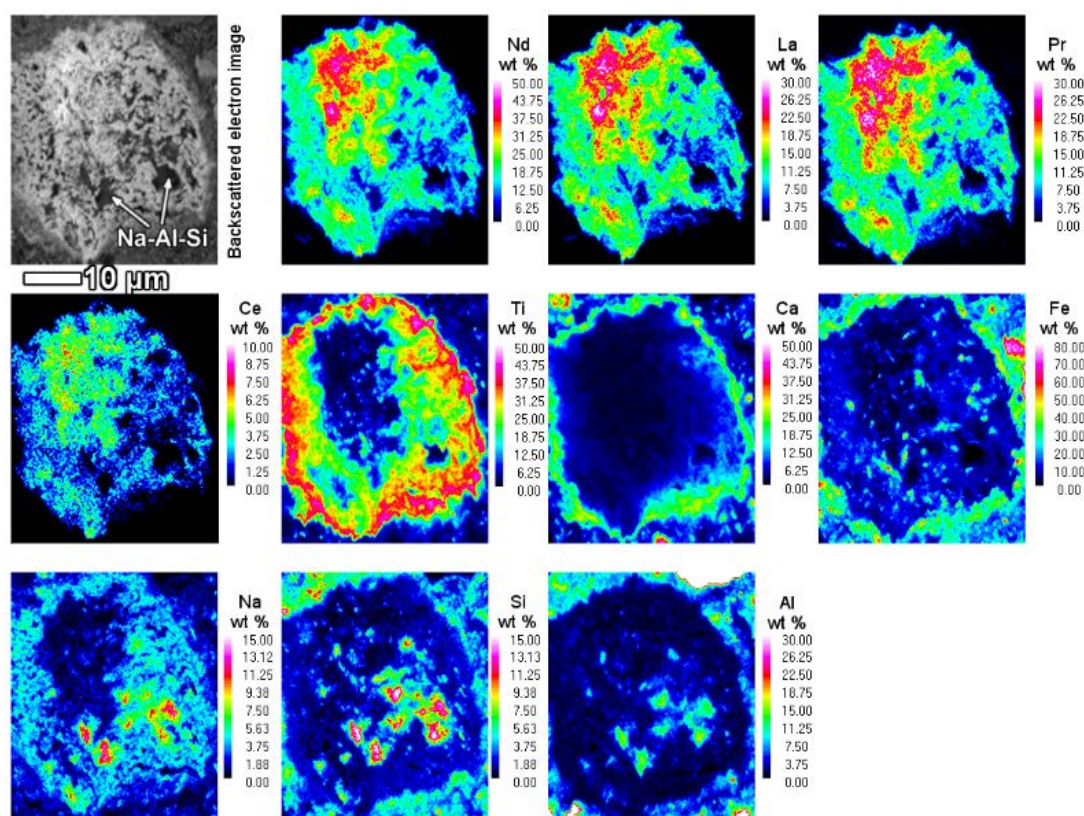


Figure 11. EPMA-WDS quantitative elemental mapping of a reacted LREE particle. The intensely reacted area is also intergrown with sodium aluminosilicate phase (indicated with Na-Al-Si). Mapped area corresponds to Figure 8(b).

A few considerations can be given about the formation mechanism of such LREE ferrotitanate phases. As mentioned before, the LREE ferrotitanate phases are clearly formed during the Bayer process. The primary LREE phases interact with the Bayer process liquor. The precursor phases possibly belong to the bastnäsite mineral group of REE fluorocarbonates or cerianite as they are the most frequently encountered LREE phases in bauxite feed. Bayer liquor consists mainly of sodium aluminate and free sodium in the form of sodium hydroxide [7]. There is commonly, at least in the high temperature process, also a small proportion of dissolved iron (3–50 mg/L Fe_2O_3) and titanium (1–10 mg/L TiO_2) present [39,79,80]. The reaction appears to take place in-situ on the outer part of the REE particles (III on Figure 8b). There is no indication if the newly formed phases would be precipitated from the processing liquor. The ions taking part in the reaction (Na, Fe, Ti, Ca) diffuse into deeper parts of the particles as the reaction progresses. Titanium ions diffusion seems to be the most intense. The inner part of the particle (I on Figure 8b) seems to be only slightly affected by the reaction, as there is only a minor part of titanium and iron present while no sodium is detected. Similarly, the particle on Figure 8a has very low content of titanium and iron as well as sodium. The presence of calcium might be already inherited from the precursor mineral. Thus, the complete particle on Figure 8a as well as inner part (I) of on Figure 8b are neither entirely a primary REE phase nor a newly created LREE ferrotitanate, but an intermediate phase with a deficiency of titanium and iron. The intensely reacted zones II and III (Figures 8b and 11) are also intergrown with sodium aluminium silicate phases. This might indicate to a gel-like state in the reaction front that allows also other mineral species to be nucleated and formed.

The morphology of the inner part resembles the fibrous or acicular radiating morphology described in the case of authigenic LREE phases in bauxites [26]. The middle and outer parts (II and III) exhibit a different morphology with globular crystallites, which are characteristic to the newly formed LREE ferrotitanates. They indicate also to a newly formed mineralogical character. The outer part (III) of the particle represents the last stage of the transformation, where a high amount of calcium and titanium have been deposited with 4–23 wt % of REEs also present (Table 6). This latest deposition forms a distinct shell around many of the observed LREE particles.

Considering that the grains on Figure 8 are relatively large, it can be assumed that smaller REE particles react entirely and their final products should be something similar to what is observed in the zone III on Figure 8b, with calcium prevailing ferrotitanates alongside some presence of REEs. We have shown evidence in support of this claim from the nanoscale HRTEM investigation, where the maximum REE concentrations per particle did not exceed 5 wt %. The particles seen in nanoscale have a similar composition as well as morphology to the area seen in highly reacted zone III on Figure 8b.

In support of the in-situ transformation of LREE minerals in the Bayer process stands the fact that LREEs do not possess soluble species in highly alkaline conditions [81,82]. In a broad sense, an analogous in situ transformation of kaolinite to sodium aluminium hydrosilicate has been described to take place during Bayer process [83].

We observed that the LREE species containing sodium, calcium, titanium and iron in variable proportions form a solid solution. The characteristics of the solid solution are expressed on Figure 12, where the ionic proportions of the cations are plotted. Region denoted with I on (a) refers to the measurements reflecting the real solid solution. Region denoted with II on (a) are the measurements performed on the transitional phases that are not the final LREE ferrotitanate products. The solid solution characteristic is the most recognizable on A site, where Ca and Na substitute REEs. The correlation coefficient between the substituting cations is 0.947 (b on Figure 12). The endmembers of the series have ideal compositions of $(\text{Ca},\text{Na})(\text{Ti},\text{Fe})\text{O}_3$ and $(\text{REE},\text{Ca},\text{Na})(\text{Ti},\text{Fe})\text{O}_3$. Because the measured compositions are highly variable, it is not reasonable to report any average chemical composition or formula of the LREE ferrotitanates. Some examples of the formulas can be shown that approach the ideal stoichiometric end-members of the series. For the neodymium-lanthanum predominant phases they can be $(\text{Ca}_{0.40}\text{Na}_{0.36}\text{REE}_{0.22})_{\Sigma 0.98}(\text{Ti}_{0.81}\text{Fe}_{0.25})_{\Sigma 1.05}\text{O}_3$ (spot 10 in Table 6) and $(\text{REE}_{0.56}\text{Na}_{0.31}\text{Ca}_{0.22})_{\Sigma 1.08}(\text{Ti}_{0.65}\text{Fe}_{0.33})_{\Sigma 0.97}\text{O}_3$ (spot 8 in Table 6).

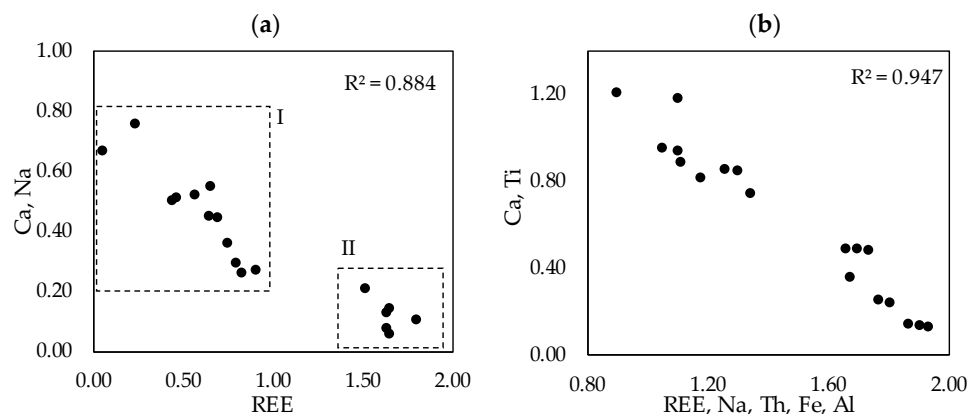


Figure 12. Solid solution character of LREE ferrotitanate series, depicted as ionic proportions of the (a) substitutions of Ca and Na with REE on A site and (b) complete transformation, where $(\text{REE} + \text{Na} + \text{Th}) + (\text{Fe} + \text{Al}) = \text{Ca} + \text{Ti}$. Region annotated with I on (a) refers to the area of real solid solution, region annotated with II on (a) indicates to the measurements on transitional phases. Adapted after Campbell et al. and Nickel & McAdam [77,84]. The equation is changed for a best description of present situation (i.e., Nb is left out of the equation whilst Th and Al are added to A and B sites, respectively). Figures are based on data from Tables 5 and 6.

The only mineral group containing species corresponding to the currently presented chemical composition (Tables 5 and 6) is the perovskite *sensu lato*. Perovskite group, also termed as the perovskite supergroup refers to the basic structure of ABX_3 , where A is a relatively large cation, B is relatively small cation and X is oxygen or another anion [76]. It's aristotypic mineral structure is cubic. However, due to the extremely wide compositional variations, many structures are possible. Perovskites exhibit extensive solid solutions, where diverse cations can occupy the A and B sites. REE-containing perovskites are well known from the natural systems and there have been a large number of REE perovskites synthesized for many applications [76,85,86]. The compositions measured in present work resemble the end-members of the perovskite *sensu stricto* (CaTiO_3) and loparite ($(\text{REE}, \text{Na}, \text{Ca})(\text{Ti}, \text{Nb})\text{O}_3$) [87] solid solution series [76]. Loparite typically occurs in peralkaline igneous rocks, especially in nepheline syenite [87]. As in the peralkaline rocks, there is an excess of sodium in the present investigated system of Bayer process. It can be noted from Tables 5 and 6, that the currently calculated mineral formulas don't have an ideal stoichiometry as there are deficiencies and excesses of ions on A and B sites. This is a regularly encountered observation for perovskites, as they are considered "defect" structures [76,77]. Excess and deficiency are compensated with the different ion proportions on A and B sites considering the charge balance as well as excess or deficiency of oxygen molecules [76,77,85]. As many of currently analysed spots show approximately 1:1 ratio of A:B sites, oxygen deficiency can be hypothesised to exist. One of the deviations compared to perovskite-loparite natural system, however, is that in current observations, there is no presence of niobium detected. Typically, niobium is a ubiquitous constituent in the natural occurrences of loparite [76]. This is explained by the fact that present LREE ferrotitanates are formed in-situ and thus inherit partly the chemical composition of their precursor phases. In the precursor minerals, there is no niobium present (Table 4). Besides, niobium concentration in the bulk sample is low, 100 mg/kg (Table 3). Thus, niobium is not expected to appear in the reaction product either. A second slight deviation is, that we are also observing the presence of iron in the analysed particles. However, iron can generally exist together with titanium on the B site of perovskite/loparite [77], but the nomenclature of iron containing perovskites has not yet been established [76]. Regardless of the incomplete nomenclature, perovskites with composition LaFeO_3 have been synthesized and characterised [88]. Since we are investigating a technogenic system and not a natural one, it is not uncommon to find some rarely encountered mineral types. Perovskites matching with the currently defined chemical composition have not yet been

synthesised, but similar ones are for example $\text{NaLaTi}_2\text{O}_6$ or $\text{NaCeTi}_2\text{O}_6$ [76]. Moreover, endmembers of perovskite-loparite series with formulas $\text{Na}_{0.5}\text{Ce}_{0.5}\text{TiO}_3$ and $\text{Na}_{0.5}\text{La}_{0.5}\text{TiO}_3$ have been identified as thermodynamically stable [89]. Among a variety of perovskite synthesizing methods, there exist the wet chemical processes, such as hydroxide-based sol-gel process [86].

Present findings can also be related to some of the previously existing knowledge about REE phases in bauxite residue. During a nanoscale investigation, a perovskite phase with a general composition of $\text{Ca}_{0.8}\text{Na}_{0.2}\text{TiO}_3$ was described to contain trace amounts of thorium as well possibly cerium and some other trace elements [52]. The authors proposed a minor contribution from a loparite phase related to perovskite to explain the observations. That information compares well with the present analysis. The mentioned perovskite was also crystallographically characterised and matched with perovskite structure reference with some deviations from the conventional data, possibly due to the incorporation of sodium on the A site of perovskite [52]. Cerium and titanium correlating presence was found in a Canadian bauxite residue sample [53]. Bayer process derived REE titanate compounds were mentioned in a patent describing the recovery of REEs from bauxite residue [51]. A recent contribution that investigated strictly the forms of cerium in bauxite residue, did not refer to any relations between cerium and titanium [55]. The former comparison allows to suggest, that the observed LREE ferrotitanate phases presented in this study are not isolated cases for only AoG-s bauxite residue, but instead seem to be a more generic characteristic that occurs in bauxite residues originating from different alumina refineries. The exception presented by Bolanz et al., who hypothesize that the main carrier of cerium is hematite [55], indicates to the need of examining rare earth phases in relation to Bayer process conditions as well as in relation to bauxite feed and REE occurrence forms within bauxite.

Current data supports the existence of thorium in perovskite type phases contained in bauxite residue [52]. In fact, compared to the 700 mg/kg thorium concentration estimated in the report by Gamaletsos et al. [52] based on EDS analysis, our WDS quantification results show that thorium concentration in cerium predominant LREE ferrotitanates can reach as high as 2.7 wt % ThO_2 (Table 5). Also, thorium is mainly associated with cerium predominant phases instead of neodymium and lanthanum predominant ones. This can be explained by the possible existence of cerium in tetravalent oxidation state, which is the same as for thorium. At the same time, practically all the other REEs occur only in the trivalent oxidation state. That inhibits the incorporation of thorium to the mineral structure of neodymium predominant phases. The amount of thorium incorporated to LREE ferrotitanate phases is probably highly dependent on the precursor REE phases in bauxite and the content of thorium within them.

Our observations deviate with the work of Gamaletsos et al. [52] in the fact that no niobium or zirconium were detected in the LREE ferrotitanate particles analysed in this work. Considering the reaction mechanism that forms the LREE ferrotitanates, it is a reasonable observation that the aforementioned elements are not present in the reacted REE particles since neither of them is a component of the precursor REE phases. Current work also disagrees with the statement of Gamaletsos et al. [52], that bauxite residue is a very homogeneous material, for which microscale investigations, especially with regards of trace elements, are not feasible to be conducted. As shown in present work, microscale investigations, combined with nanoscale analysis, provide very detailed information about the fate of REE minerals in the Bayer process.

6.3.3. Manganese-Associated Cerium Oxide or Oxyhydroxide

A part of LREE phases were found to be associated with manganese (Mn) in bauxite residue (Figure 13). On Figure 13 and similar observations, LREEs occur as surface adsorbed phases on manganese mineral particles. It may be assumed that they are manganese oxyhydroxides. In the case of the particles depicted on Figure 13 as well as Figure 14, the manganese particle is also associated with cobalt (Co) and nickel (Ni) as well as some magnesium (Mg). Following its chemical composition, the manganese phase could be asbolane $(\text{Mn}(\text{O},\text{OH})_2(\text{Ni},\text{Co})_x(\text{O},\text{OH})_2 \cdot n\text{H}_2\text{O})$ [90].

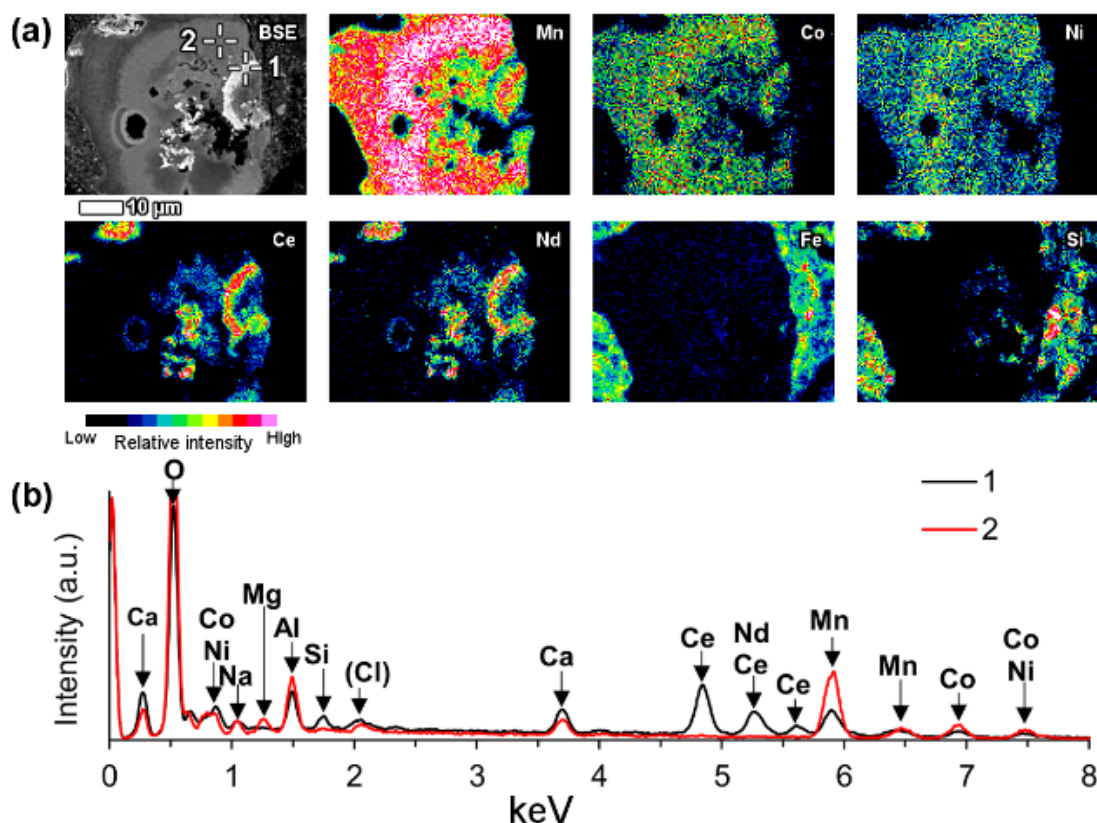


Figure 13. Cerium oxide/oxyhydroxide phase associated with manganese particle shown on (a) EDS elemental map with (b) respective spectra.

It is common that the named LREE formations have a circular morphology that follows the circular cavities of manganese particles or they surround the manganese grains. The mentioned LREE phases contain cerium as the prevailing element, but other lanthanides as well as calcium were discerned to be present also (Figure 13). Based on semi-quantitative EDS estimation, cerium concentration in this LREE occurrence form is about 35–40 wt %.

Individual manganese associated LREE particles are small, about 1 μm in size, but agglomerated particles are over 10 μm in dimensions. On occasions, manganese associated LREE phases exhibit remarkable sizes exceeding 50 μm (Figure 14). On the example of the particle depicted on Figure 14, it may be assumed that the growth of this LREE particle was nucleated on a manganese-nickel-cobalt particle and continued to form a cerium and calcium predominant particle. The fine acicular morphology of the particle on Figure 14 indicates that the growth rate of this particle has been relatively fast.

LREE phases of this category do not exhibit the presence phosphorus or carbon (measured in platinum-coated sample). Therefore, the occurrence form as phosphate or carbonate can be excluded. The absence of titanium, iron or sodium and a different morphology compared to LREE ferrotitanates (Section 6.3.2) rules out the linkages between the LREE ferrotitanate forms. As a conclusion, these LREE phases can be termed as oxides or oxyhydroxides, which might correspond to cerianite.

Laskou and Andreou [28] have referred to the existence of minor amounts of manganese oxyhydroxides, as well as lithioporite and brindleyite, in the Parnassos-Ghiona bauxite profiles. It is possible that these are the precursor manganese phases for the kinds observed in bauxite residue in present study. Higher REE concentrations have been noted to occur together with higher manganese concentrations in Parnassos-Ghiona bauxite profiles [91], while some authors have noted a negative correlation between the REEs and manganese contents [28]. Nevertheless, relations of these manganese

phases with specific REE minerals in Parnassos-Ghiona bauxites have not been noted. Even more, such manganese-associated REE occurrences have not been noted in any bauxite deposit.

Manganese and REEs are chemically similar and in natural systems, manganese-adsorbed REEs are not uncommonly encountered, especially in marine environment [92]. There, REEs occur in the form of adsorption onto ferro-manganese crusts and nodules [93,94]. It is worth mentioning that similar cerium occurrence form has been revealed in nickel laterites from Dominican Republic. Rings of cerianite in the sizes of about 5 μm or larger aggregates up to 30 μm were associated with manganese oxyhydroxides [95]. The morphology of those cerianite occurrence forms resembles the morphology seen in present work.

Considering that the described LREE occurrence form has only been observed in bauxite residue and its morphology indicates to a relatively fast crystallisation, we assume that this might be a secondary form of LREE occurrence, created during the Bayer process. An easily leachable REE occurrence form by ion-adsorption, related possibly to kaolinite, illite or chamosite, has been speculated to exist in Parnassos-Ghiona bauxites [72]. This claim has some support from present investigation (Figure 2). It might be that the ion-adsorbed REEs are leached during the Bayer digestion and are thereafter precipitated in association with manganese particles. From the relative abundance of cerium compared to other lanthanides in these specimens, it can be assumed that cerium occurs in the tetravalent oxidation state. Similarly, the most common oxidation state of manganese is 4^+ (also 2^+), allowing a more favourable co-occurrence of these metals.

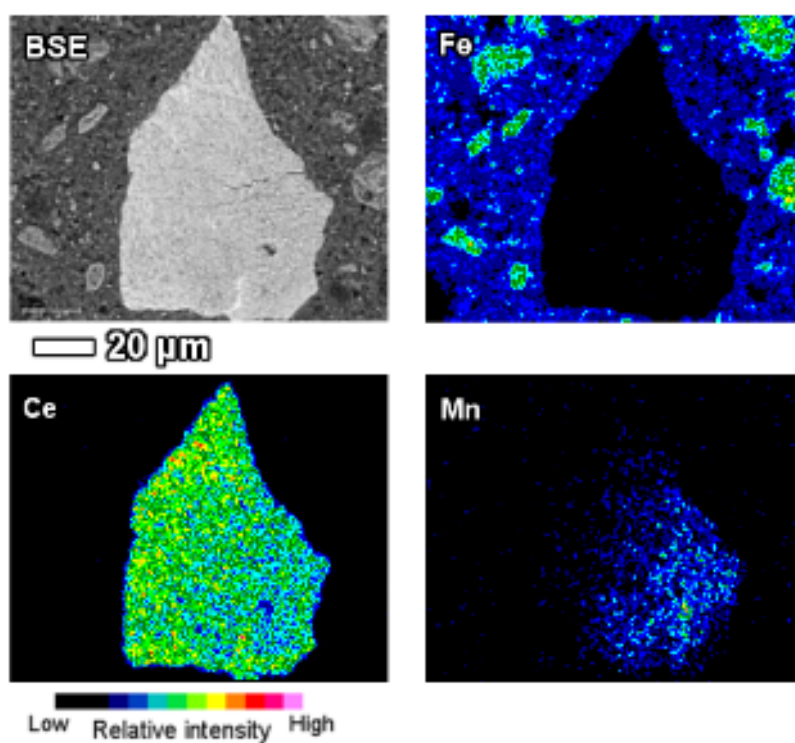


Figure 14. Cerium oxide/oxyhydroxide phase associated with manganese.

6.3.4. Heavy REE Phosphates

Heavy rare earth phosphates with the major constituent being yttrium were found in bauxite residue (Figure 15). Other HREEs like gadolinium, dysprosium and erbium were also present. These phases correspond to xenotime or churchite. Xenotime particles are a few μm in size. They can be either contained in a diaspore/boehmite particle (Figure 15) or with a free surface inside bauxite residue matrix. Either way, protected by another particle or not, xenotime/churchite endures the Bayer digestion conditions. It appears in bauxite residue in its original form just as in bauxite ores [28].

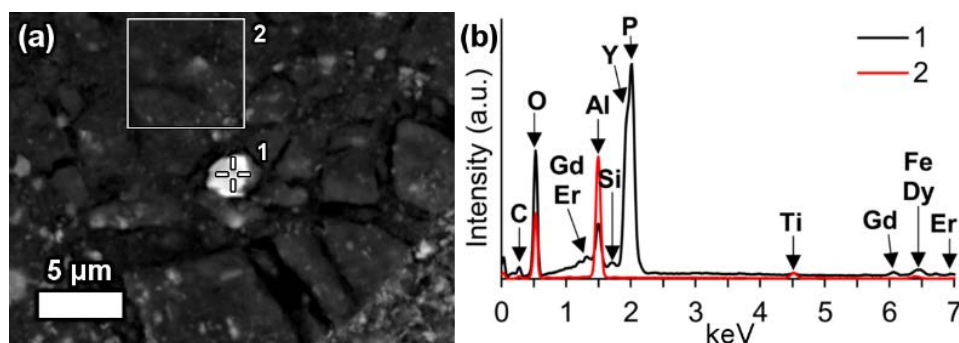


Figure 15. Xenotime or churchite in undigested diaspore/boehmite matrix, depicted on (a) backscattered electron image with its (b) EDS spectrum.

6.3.5. Mixed REE Occurrences

Some REE particles were found as mixtures of different REE species. One example of such particle is depicted on Figure 16. It contains cerium as the prevailing REE, while it also contains neodymium, lanthanum, calcium as well as minor yttrium and thorium (Figure 16b). The particle could be either a LREE carbonate or an oxide/oxyhydroxide phase. What makes it different from the formerly described observations is that it also contains phosphorus, indicating to the presence of REE phosphate phases within a mixed type of REE particle.

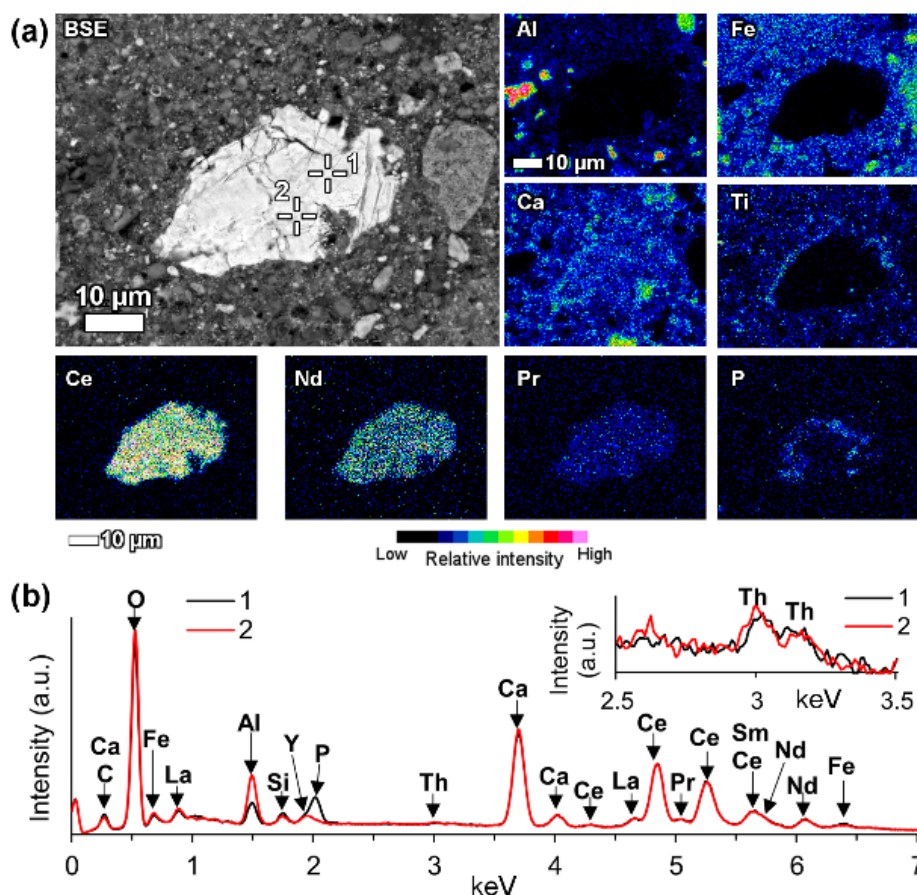


Figure 16. A mixed type REE particle shown on (a) backscattered electron image with respective EDS elemental maps and (b) EDS spectrograms corresponding to indicated spot analyses.

Another example of a mixed REE particle is depicted on Figure 17. The important characteristic of this particle is that the REEs are contained within the pores and fissures of a large iron oxide particle. The iron oxide particle has acted as a protective shield from the Bayer liquor and therefore the REE phases contained within it are thought to be primary ones, inherited from bauxite. In present case, neodymium is the prevailing metal in the regions of REEs presence, seconded by lanthanum. Like the previously described particle in Figure 16, this particle (Figure 17) also exhibits the partial presence of phosphorous. The total area with neodymium presence does not coincide with the presence of phosphorus, but all areas shown to contain phosphorus, coincide with the occurrence of neodymium. Therefore, the primary LREE phases contained within the fissures and pores of the iron oxide particle are LREE phosphates and possibly carbonates.

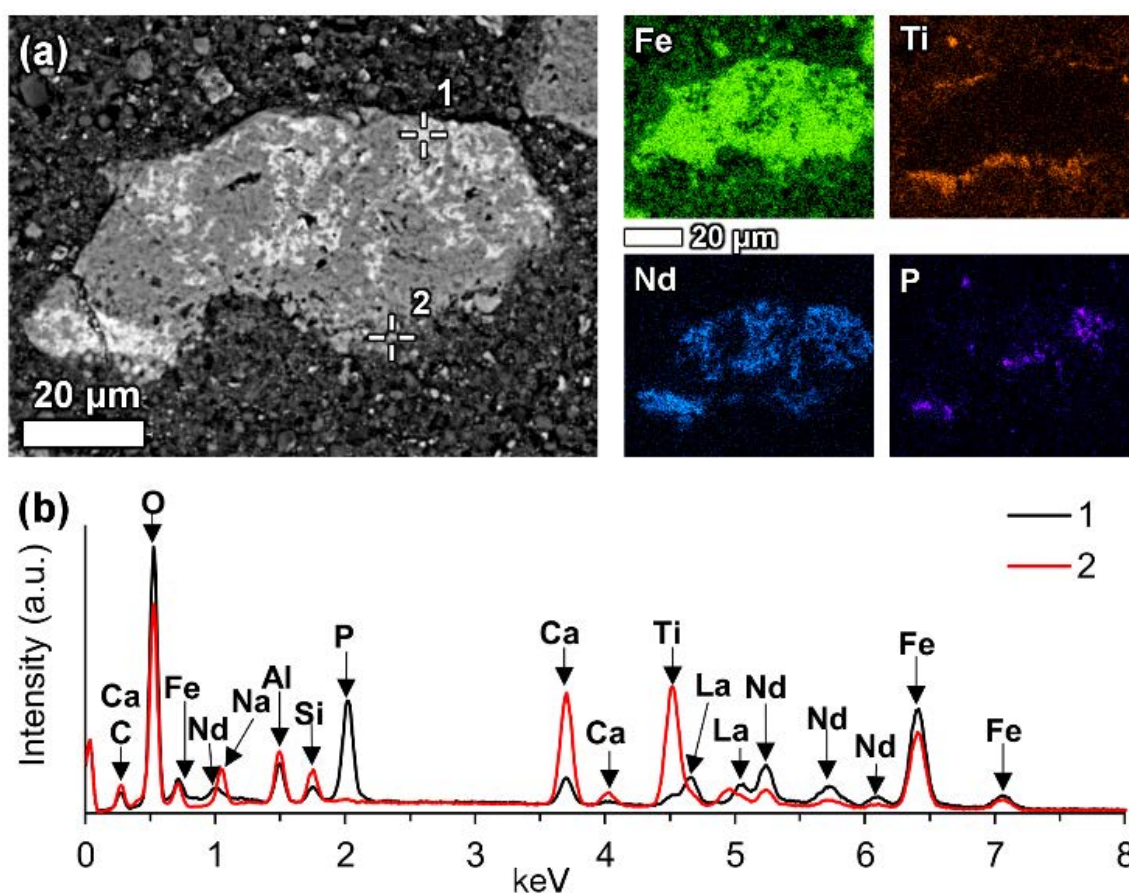


Figure 17. Mixed LREE phases entrapped in iron oxide grain depicted on (a) backscattered electron image and respective EDS elemental maps and (b) corresponding EDS spectra. Element maps are monochromatic, thus there is no colour intensity scale.

Both previously described particles share the characteristic that they are partially surrounded by a calcium ferrotitanate shell or a rim, where minor LREE content is also present (Figures 16 and 17b). This indicates that the particles passing through the Bayer process are slightly affected by the caustic digestion. It also concludes that the majority of LREE particles found in bauxite residue are surrounded by a calcium ferrotitanate rim that has been formed during the Bayer process.

6.4. Summary of REE Phases Physical Parameters

It is not feasible to quantify how much of each REE phase is present in bauxite residue. However, hereby we have summarised the observations in Table 7 and classified them according to previously presented categories (Section 6.3). The most frequently encountered REE particles are LREE

ferrotitanates. This concludes that the majority of REE particles entering to the process are affected by Bayer digestion. The typical sizes of the LREE particles are 5–10 μm . HREE particles tend to be smaller, 2–3 μm . Low REEs content ferrotitanate category refers to observations with REE concentration below 5 wt %. They are mainly encountered in the very fine particulate (<1 μm) of bauxite residue, revealed by HRTEM-EDS.

Table 7. Summary of the physical parameters of the encountered REE particles in bauxite residue.

Phase	Count	Typical Size (μm)	Free Surface/Total Count
LREE carbonate	1	20–30	1/1
Yttrium phosphate (xenotime/churchite)	3	2–3	2/3
Cerium phosphate	3	5–10	2/3
Partly reacted LREE ferrotitanate	4	10	4/4
High LREE content (>5 wt %) ferrotitanate	16	5–10	15/16
Low LREE content (<5 wt %) ferrotitanate	6	<1	6/6
Cerium oxide/oxyhydroxide	1	5	0/1
Cerium oxide/oxyhydr. associated with manganese	3	irregular	2/3
Mixed	3	20–40	1/3

We also summarised the proportions of the REE particles having a free surface. This excludes the fact that many of the observed particles are surrounded by a calcium ferrotitanate rim. It was concluded that the majority of REE particles have a free surface. The particles might be covered only by a fine bauxite residue particulate coating, but this is likely not a chemical association. Such occurrences that are categorized as “mixed” tend to be more entrapped in some other major mineral particle, as seen on Figure 17.

Microscale investigation resulted in finding a remarkable number of discrete REE particles with substantially higher REEs concentration in relation to their bulk concentration in the sample. Nanoscale assessment discerned the existence of calcium ferrotitanate phases with several weight percent REEs concentrations, that also surpass REEs bulk concentration in bauxite residue. Current work does not provide support for the suggestion by Bolanz et al. [55] who speculated that tetravalent cerium could theoretically be located in bauxite residue within hematite lattice. Neither does present work disprove the existence of such occurrence forms.

7. Considerations for the Recovery of REEs from Bauxite Residue

Since the mineralogical character of REEs in bauxite residue has been elucidated, some considerations for the recovery of REEs can be suggested. The most abundant REE type identified in this work is LREE ferrotitanate. It resembles mostly the naturally occurring loparite mineral, $(\text{REE}, \text{Ca})(\text{Ti}, \text{Nb})\text{O}_3$. Loparite is currently exploited only in the Lovozero massif (Kola peninsula, Russia) [87]. This mineral is being beneficiated there with the combination of density and magnetic separation methods [96]. Thus, additional physical beneficiation methods could be explored also for bauxite residue, based on the existing knowledge about loparite beneficiation. In support of this proposal is the fact that the majority of REE particles in bauxite residue are not attached to other mineral particles, i.e., they have a free surface. However, the beneficiation trials so far have not been very encouraging [11] and a likely restriction is the similar density of hematite (5.26–5.30 g/cm^3) and loparite (4.77 g/cm^3) known from natural systems. The recovery of REEs from Lovozero loparite is performed via pyrometallurgical route by chlorination [87]. Chlorination has been trialled in the case of bauxite residue [11], but this route could be developed further.

On the one hand, the observed REE particles have commonly a free surface, therefore they should be immediately affected by any treatment performed targeting the leaching of REE phases from bauxite residue. On the other hand, the newly formed LREE ferrotitanate particles tend to have a calcium ferrotitanate shell surrounding them. The indicated shells might hinder the effectiveness of leaching performance due to the need of dissolving the titanate shell before the reaction reaches to the area with high REEs concentrations.

Another approach for discussing these matters is to compare REE phases found in bauxite and in bauxite residue. In metallurgical terms, the REE fluorocarbonates that are found in bauxites should be easier to be processed compared to the complex LREE ferrotitanate phases in bauxite residue. Thus, the route of recovering REEs from crushed bauxite before Bayer digestion is encouraged to be tested. In support of the latter, Mouchos et al. [72] have demonstrated that between 19% and 47% of REEs in bauxite are easily leachable, in fact ion exchangeable, using ammonium sulphate. They also proposed an option to selectively mine the REE-enriched lower parts of bauxite deposits and thus recover REEs prior to Bayer process [72]. Our mineralogical assessment supports such an approach, as the REE phases in bauxite are less complex than in bauxite residue.

The fact that thorium is associated with LREE phases, particularly with cerium predominant ferrotitanates, indicates to a possible route of removing thorium from the system. If REE leaching from bauxite residue is performed, thorium should also be leached because of its presence in the same mineral phases as the REEs. The simultaneous dissolution of REEs and thorium is a well-documented behaviour in the REEs industry [33]. This so far has not been identified in the case of bauxite residue [11]. The possible leaching of thorium along with REEs could be potentially beneficial for the use of leached bauxite residue in construction materials. Naturally occurring thorium with its radionuclide series is the main source of ionising radiation related to bauxite residue, that puts certain limits to the re-use of this material in construction applications in its raw form [97,98].

8. Conclusions

A careful and dedicated investigation of bauxite residue by EPMA and HRTEM revealed that there are several types of discrete REE phases contained in bauxite residue. The most abundant of them is a LREE ferrotitanate (REE,Ca,Na)(Ti,Fe)O₃ phase, that chemically resembles the naturally occurring loparite except for the absence of niobium. However, plenty of synthetic REE perovskite compounds exist that are like the LREE ferrotitanates observed in the present study. LREE ferrotitanates form a solid solution between the ideal end-members (Ca,Na)(Ti,Fe)O₃ and (REE,Ca,Na)(Ti,Fe)O₃. These occurrences further sub-divide into cerium predominant and neodymium-lanthanum predominant types. The cerium predominant form also contains up to 2.7 wt % thorium. Calcium ferrotitanate particles with low LREE concentration (<5 wt %) are rather concentrated into the very fine (<1 µm) particulates of bauxite residue. LREE ferrotitanates are formed during the Bayer process digestion by an in-situ transformation of the precursor bauxite LREE minerals contained in the bauxite feed. Thus, the composition of the newly formed phases depends on (1) the chemical composition of the precursor REE phases and (2) the extent of incorporation of sodium as well as dissolved iron and titanium ions into their composition. The latest reaction products are those with the prevailing concentration of calcium and with a low (<5 wt %) LREE concentration and they are found among the nano-scaled bauxite residue particles.

Minor amounts of LREEs are found as carbonates and phosphates, referring to the partial resistance of these phases to Bayer process digestion conditions. A part of cerium and minor presence of other lanthanides were found to be associated with manganese phases in the form of adsorption on their surface or in manganese particle cavities. These occurrence forms are thought to be secondary, created from the fast precipitation of a small proportion of dissolved lanthanides.

Heavy REEs are found in bauxite residue in the same form as in bauxite, namely as yttrium phosphate phases (xenotime/churchite). Their major constituent, yttrium, is seconded by other HREEs like gadolinium, dysprosium and erbium. Some yttrium is incorporated into mixed REE phases.

The presence of Bayer process derived calcium ferrotitanate shells around LREE particles probably hinders the immediate solubility of LREE grains during REEs leaching from bauxite residue. It is likely that the complex LREE ferrotitanates dissolve less readily than LREE fluorocarbonate minerals found in bauxites.

Present work concludes that REEs are found among bauxite residue's microscale particulate as discrete phases with a high REE concentration and among nano-scaled particulate in the composition

of calcium ferrotitanate phases. We anticipate that bauxite residue or bauxite ore will become a sustainable and responsible source of REEs.

The findings presented here are currently the only explanation of REE, except for cerium, occurrences in bauxite residue. However, further work is necessary to enhance the understanding of how REEs occur in bauxite residue.

Acknowledgments: Kalle Kirsimäe and Marian Külaviir from University of Tartu are thanked for their valuable help with electron microscopy. Apostolos Kourtis from National Technical University of Athens (NTUA) is thanked for the help with μ -Raman spectroscopy. We offer thanks to Professor George Furlaris from NTUA for providing the access to HRTEM facilities. John Craven from the University of Edinburgh is thanked for providing the Nd and Pr based glass standards used for the EPMA-WDS analyses. Constructive remarks by three anonymous reviewers are greatly appreciated. The research leading to these results has received funding from the European Community's Horizon 2020 Programme (H2020/2014–2019) under Grant Agreement No. 636876 (MSCA-ETN REDMUD). This publication reflects only the authors' views, exempting the Community from any liability. Project website: <http://www.etn.redmud.org>.

Author Contributions: J.V., V.V. and D.P. conceived and designed the experiments; A.H.T. contributed to the design of the experiments and editing of the paper; J.V., A.M. and B.B. performed the EPMA-WDS experiments; J.V. performed the EPMA-EDS and μ -Raman experiments; P.E.T. and J.V. performed the HRTEM experiments; J.V. analysed the data and wrote the paper.

Conflicts of Interest: The authors declare no conflict of interest. The funding sponsors had no role in the design of the study; in the collection, analyses, or interpretation of data; in the writing of the manuscript, and in the decision to publish the results.

Appendix A

Table A1. Normalised HRTEM-EDS semi-quantitative analysis of calcium ferrotitanate particles.

Measurement No.	O	Na	Mg	Al	Si	S	Ca	Ti	V	Cr	Fe	Co	Zr	La	Ce	Nd	Th	Sum
2-22	9.6	2.4	n/a	0.9	1.6	n/a	28.3	39.2	n/a	0.6	11.0	1.1	n/a	1.8	3.3	0.2	n/a	100.0
4-23	24.6	2.9	n/a	0.6	1.5	n/a	26.8	36.3	0.5	n/a	5.2	n/a	n/a	0.1	1.4	0.0	n/a	100.0
2-24	25.8	1.7	n/a	4.4	5.4	0.4	15.9	21.2	n/a	0.8	23.1	n/a	n/a	0.0	0.8	0.5	n/a	100.0
3-24	21.6	3.2	n/a	0.6	1.7	n/a	29.5	38.6	n/a	n/a	2.1	0.2	n/a	0.0	2.1	0.3	n/a	100.0
2-58	19.5	2.4	n/a	0.9	1.4	n/a	25.2	32.0	n/a	0.6	14.0	n/a	n/a	2.8	0.9	0.2	n/a	100.0
4-25	17.9	2.0	n/a	1.1	1.6	n/a	31.8	40.3	0.7	n/a	3.4	n/a	n/a	0.0	1.1	0.0	n/a	100.0
2-57	10.5	2.9	n/a	0.9	2.1	n/a	33.1	41.7	n/a	0.6	2.9	1.1	n/a	0.9	2.8	0.1	0.4	100.0
3-7	21.1	1.7	n/a	0.6	1.6	n/a	28.6	35.6	n/a	n/a	10.1	n/a	n/a	0.0	0.6	0.0	n/a	100.0
2-41	17.7	2.4	n/a	1.0	1.7	n/a	25.1	31.0	n/a	0.7	18.0	1.0	n/a	0.0	0.9	0.2	0.4	100.0
3-63	3.9	1.4	n/a	1.0	2.0	n/a	39.6	47.7	n/a	0.4	3.4	n/a	n/a	0.0	0.5	0.2	n/a	100.0
2-42	11.5	1.2	n/a	0.8	1.6	n/a	26.9	32.2	n/a	0.8	23.9	n/a	n/a	0.0	0.4	0.3	0.4	100.0
2-14	23.1	2.6	n/a	n/a	2.1	n/a	31.1	36.9	n/a	0.5	2.7	n/a	n/a	0.5	0.3	0.2	n/a	100.0
2-21	19.8	2.7	n/a	0.9	1.6	n/a	29.5	34.9	n/a	0.7	8.1	0.9	n/a	0.4	0.6	0.1	n/a	100.0
2-15	14.8	1.4	n/a	1.6	1.5	n/a	26.8	31.4	n/a	0.6	21.6	n/a	n/a	0.0	0.2	0.1	n/a	100.0
3-6	12.8	0.8	n/a	0.7	1.2	n/a	27.4	32.0	n/a	0.6	24.1	n/a	n/a	0.0	0.4	0.1	n/a	100.0
3-69	16.9	2.4	1.0	1.9	n/a	n/a	32.7	38.0	n/a	n/a	3.1	n/a	0.6	2.6	0.8	0.0	n/a	100.0
2-71	27.2	2.9	n/a	1.5	1.7	n/a	27.9	32.1	n/a	0.6	2.8	0.9	n/a	1.5	0.8	0.0	n/a	100.0
1-17	33.9	1.6	n/a	3.9	2.9	n/a	20.6	18.5	n/a	0.4	17.7	n/a	n/a	n/a	0.5	n/a	n/a	100.0
4-9	24.2	n/a	n/a	n/a	1.9	n/a	32.8	37.1	0.5	n/a	2.5	n/a	0.5	n/a	0.5	0.0	n/a	100.0

References

1. Ripple, W.J.; Wolf, C.; Newsome, T.M.; Galetti, M.; Alamgir, M.; Crist, E.; Mahmoud, M.I.; Laurance, W.F. World scientists' warning to humanity: A second notice. *BioScience* **2017**, *67*, 1026–1028. [\[CrossRef\]](#)
2. Ali, S.H. Social and environmental impact of the rare earth industries. *Resources* **2014**, *3*, 123–134. [\[CrossRef\]](#)
3. Wall, F.; Rollat, A.; Pell, R.S. Responsible sourcing of critical metals. *Elements* **2017**, *13*, 313–318. [\[CrossRef\]](#)
4. Atwood, D.A. *The Rare Earth Elements: Fundamentals and Applications*; John Wiley & Sons: Hoboken, NJ, USA, 2013; ISBN 1-118-63263-X.
5. Samson, I.M.; Chassé, M. Scandium. In *Encyclopedia of Geochemistry*; White, W.M., Ed.; Encyclopedia of Earth Sciences Series; Springer International Publishing: Berlin, Germany, 2016; pp. 1–5; ISBN 978-3-319-39193-9.
6. Suss, A.; Kuznetsova, N.V.; Kozyrev, A.; Panov, A.; Gorbachev, S. Specific features of scandium behavior during sodium bicarbonate digestion of red mud. In Proceedings of the 35th International Conference and Exhibition of ICSOBA (Travaux 46), Hamburg, Germany, 2–5 October 2017; pp. 491–504.
7. Power, G.; Gräfe, M.; Klauber, C. Bauxite residue issues: I. Current management, disposal and storage practices. *Hydrometallurgy* **2011**, *108*, 33–45. [\[CrossRef\]](#)
8. Evans, K. The history, challenges, and new developments in the management and use of bauxite residue. *J. Sustain. Metall.* **2016**, *2*, 316–331. [\[CrossRef\]](#)
9. Mayes, W.M.; Burke, I.T.; Gomes, H.I.; Anton, Á.D.; Molnár, M.; Feigl, V.; Ujaczki, É. Advances in understanding environmental risks of red mud after the Ajka spill, Hungary. *J. Sustain. Metall.* **2016**, *2*, 332–343. [\[CrossRef\]](#)
10. Binnemans, K.; Jones, P.T.; Blanpain, B.; Van Gerven, T.; Pontikes, Y. Towards zero-waste valorisation of rare-earth-containing industrial process residues: A critical review. *J. Clean. Prod.* **2015**, *99*, 17–38. [\[CrossRef\]](#)
11. Borra, C.R.; Blanpain, B.; Pontikes, Y.; Binnemans, K.; Van Gerven, T. Recovery of rare earths and other valuable metals from bauxite residue (red mud): A review. *J. Sustain. Metall.* **2016**, *2*, 365–386. [\[CrossRef\]](#)
12. Goodenough, K.M.; Wall, F.; Merriman, D. The rare earth elements: Demand, global resources, and challenges for resourcing future generations. *Nat. Resour. Res.* **2017**, 1–16. [\[CrossRef\]](#)
13. European Commission; Deloitte Sustainability; TNO; British Geological Survey; Bureau de Recherches Géologiques et Minières. *Study on the Review of the List of Critical Raw Materials*; Publications Office of the European Union: Luxembourg, 2017; p. 93.
14. Binnemans, K.; Jones, P.T. Rare earths and the balance problem. *J. Sustain. Metall.* **2015**, *1*, 29–38. [\[CrossRef\]](#)
15. Dedy, É.A.; Mouchos, E.; Goodenough, K.; Williamson, B.J.; Wall, F. A review of the potential for rare-earth element resources from European red muds: Examples from Seydişehir, Turkey and Parnassos-Giona, Greece. *Mineral. Mag.* **2016**, *80*, 43–61. [\[CrossRef\]](#)
16. Radusinović, S.; Jelenković, R.; Pačevski, A.; Simić, V.; Božović, D.; Holclajtner-Antunović, I.; Životić, D. Content and mode of occurrences of rare earth elements in the Zagrad karstic bauxite deposit (Nikšić area, Montenegro). *Ore Geol. Rev.* **2017**, *80*, 406–428. [\[CrossRef\]](#)
17. Valetton, I. Developments in Soil Science 1. In *Bauxites*; Elsevier: Amsterdam, The Netherlands, 1972; ISBN 978-0-444-40888-4.
18. Meyer, F.M. Availability of bauxite reserves. *Nat. Resour. Res.* **2004**, *13*, 161–172. [\[CrossRef\]](#)
19. Bárdossy, G. Developments in Economic Geology 14. In *Karst Bauxites: Bauxite Deposits on Carbonate Rocks*; Elsevier: Amsterdam, The Netherlands, 1982; ISBN 978-0-444-99727-2.
20. Valetton, I.; Biermann, M.; Reche, R.; Rosenberg, F. Genesis of nickel laterites and bauxites in Greece during the Jurassic and Cretaceous, and their relation to ultrabasic parent rocks. *Ore Geol. Rev.* **1987**, *2*, 359–404. [\[CrossRef\]](#)
21. Laskou, M.; Economou-Eliopoulos, M. The role of microorganisms on the mineralogical and geochemical characteristics of the Parnassos-Ghiona bauxite deposits, Greece. *J. Geochem. Explor.* **2007**, *93*, 67–77. [\[CrossRef\]](#)
22. Maksimović, Z.; Panto, G. Contribution to the geochemistry of the rare earth elements in the karst-bauxite deposits of Yugoslavia and Greece. *Geoderma* **1991**, *51*, 93–109. [\[CrossRef\]](#)
23. Ochsenkühn-Petropoulou, M.; Ochsenkühn, K.; Luck, J. Comparison of inductively coupled plasma mass spectrometry with inductively coupled plasma atomic emission spectrometry and instrumental neutron activation analysis for the determination of rare earth elements in Greek bauxites. *Spectrochim. Acta Part B At. Spectrosc.* **1991**, *46*, 51–65. [\[CrossRef\]](#)

24. Ochsenkühn-Petropulu, M.; Ochsenkühn, K.M. Rare earth minerals found in Greek bauxites by scanning electron microscopy and electron probe micro-analysis. *Microsc. Anal.* **1995**, *37*, 33–34.
25. Maksimović, Z.; Panto, G. Bastnäsite-(La) and monazite-(Nd): A new variety of monazite from the Marmara bauxite deposit (Greece). *Bull. Acad. Serbe Sci. Arts* **1980**, *20*, 35–42.
26. Mongelli, G. Ce-anomalies in the textural components of Upper Cretaceous karst bauxites from the Apulian carbonate platform (southern Italy). *Chem. Geol.* **1997**, *140*, 69–79. [[CrossRef](#)]
27. Bárdossy, G.; Pantó, G. Trace mineral and element investigation in bauxites by electron-probe. In Proceedings of the 3rd International Congress of ICSOBA, Nice, France, 17–21 September 1973; pp. 47–53.
28. Laskou, M.; Andreou, G. Rare earth elements distribution and REE-minerals from the Parnassos–Ghiona bauxite deposits, Greece. In Proceedings of the 7th Biennial SGA Meeting on Mineral Exploration and Sustainable Development, Athens, Greece, 24–28 August 2003; pp. 89–92.
29. Maksimovic, Z.; Pantó, G. Authigenic rare earth minerals in karst-bauxites and karstic nickel deposits. In *Rare Earth Minerals: Chemistry, Origin and Ore Deposits*; Jones, A.P., Wall, F., Williams, C.T., Eds.; Mineralogical Society Series; Chapman & Hall: London, UK, 1996; Volume 7, pp. 257–280, ISBN 0 412 61030 2.
30. Wang, Q.; Deng, J.; Liu, X.; Zhang, Q.; Sun, S.; Jiang, C.; Zhou, F. Discovery of the REE minerals and its geological significance in the Quyang bauxite deposit, West Guangxi, China. *J. Asian Earth Sci.* **2010**, *39*, 701–712. [[CrossRef](#)]
31. Li, Z.; Din, J.; Xu, J.; Liao, C.; Yin, F.; Lü, T.; Cheng, L.; Li, J. Discovery of the REE minerals in the Wulong–Nanchuan bauxite deposits, Chongqing, China: Insights on conditions of formation and processes. *J. Geochem. Explor.* **2013**, *133*, 88–102. [[CrossRef](#)]
32. Proenza, J.; Aiglsperger, T.; Villanova-de-Benavent, C.; Torró i Abat, L.; Rodríguez-García, D.; Ramírez, A.; Rodríguez Servicio, J.; Nacional, G.; Republic, D. Discovery of REE minerals hosted in karst bauxite ores from the Sierra de Bahoruco, Pedernales, Dominican Republic. In Proceedings of the 14th SGA Biennial Meeting: Mineral Resources to Discover, Québec City, QC, Canada, 20–23 August 2017; Volume 4, pp. 1321–1324.
33. Habashi, F. Extractive metallurgy of rare earths. *Can. Metall. Q.* **2013**, *52*, 224–233. [[CrossRef](#)]
34. Bayer, K.J. A Process for the Production of Aluminum Hydroxide. Germany Patent 43977, 3 August 1888.
35. Bayer, K.J. A Process for the Production of Aluminum Hydroxide. Germany Patent 65604, 3 November 1892.
36. Habashi, F. A hundred years of the Bayer process for alumina production. In Proceedings of the TMS Annual Meeting, Phoenix, AZ, USA, 25–28 January 1988; pp. 3–11.
37. Das, S.K.; Yin, W. The worldwide aluminum economy: The current state of the industry. *JOM* **2007**, *59*, 57–63. [[CrossRef](#)]
38. Chin, L.A.D. The state-of-the-art in Bayer process technology. In Proceedings of the TMS Annual Meeting, Phoenix, AZ, USA, 25–28 January 1988; pp. 49–53.
39. Authier-Martin, M.; Forte, G.; Ostap, S.; See, J. The mineralogy of bauxite for producing smelter-grade alumina. *JOM* **2001**, *53*, 36–40. [[CrossRef](#)]
40. Balomenos, E.; Giannopoulou, I.; Panias, D.; Paspaliaris, I. ENEXAL: Novel technologies for enhanced energy and exergy efficiencies in primary aluminium production industry. *Metalurgija* **2009**, *15*, 203–217.
41. Lavalou, E.; Bosca, B.; Keramidas, O. Alumina production from diasporic bauxites. *Light Met.* **1999**, 55–62.
42. Derevyankin, V.A.; Porotnikova, T.P.; Kocherova, E.K.; Yumasheva, I.V.; Moiseev, V.E. Behaviour of scandium and lanthanum in the production of alumina from bauxite. *Izv. Vysshikh Uchebnykh Zaved. Tsvetnaya Metall.* **1981**, 86–89.
43. Vind, J.; Vassiliadou, V.; Panias, D. Distribution of trace elements through the Bayer process and its by-products. In Proceedings of the 35th International ICSOBA Conference (Travaux 46), Hamburg, Germany, 2–5 October 2017; pp. 255–267.
44. Wagh, A.S.; Pinnock, W.R. Occurrence of scandium and rare earth elements in Jamaican bauxite waste. *Econ. Geol.* **1987**, *82*, 757–761. [[CrossRef](#)]
45. Ochsenkühn-Petropulu, M.; Lyberopulu, T.; Parissakis, G. Direct determination of lanthanides, yttrium and scandium in bauxites and red mud from alumina production. *Anal. Chim. Acta* **1994**, *296*, 305–313. [[CrossRef](#)]
46. Davris, P.; Balomenos, E.; Taxiarchou, M.; Panias, D.; Paspaliaris, I. Current and alternative routes in the production of rare earth elements. *BHM Berg Hüttenmänn. Monatshefte* **2017**, 1–7. [[CrossRef](#)]

47. Logomerac, V.G. Distribution of rare-earth and minor elements in some bauxite and red mud produced. In Proceedings of the Second International Symposium of ICSOBA, Budapest, Hungary, 6–10 October 1971; Volume 3, pp. 383–393.
48. Borra, C.R.; Pontikes, Y.; Binnemans, K.; Van Gerven, T. Leaching of rare earths from bauxite residue (red mud). *Miner. Eng.* **2015**, *76*, 20–27. [[CrossRef](#)]
49. Ochsenkühn-Petropulu, M.; Lyberopulu, T.; Ochsenkühn, K.M.; Parissakis, G. Recovery of lanthanides and yttrium from red mud by selective leaching. *Anal. Chim. Acta* **1996**, *319*, 249–254. [[CrossRef](#)]
50. Abhilash; Sinha, S.; Sinha, M.K.; Pandey, B.D. Extraction of lanthanum and cerium from Indian red mud. *Int. J. Miner. Process.* **2014**, *127*, 70–73. [[CrossRef](#)]
51. Sugita, K.; Kobayashi, Y.; Taguchi, Y.; Takeda, S.; Ota, Y.; Ojiri, M.; Oda, K.; Sano, H. Method of Recovering Rare-Earth Elements. U.S. Patent US20,150,086,449 A1, 7 December 2012.
52. Gamaletsos, P.N.; Godelitsas, A.; Kasama, T.; Kuzmin, A.; Lagos, M.; Mertzimekis, T.J.; Göttlicher, J.; Steininger, R.; Xanthos, S.; Pontikes, Y.; et al. The role of nano-perovskite in the negligible thorium release in seawater from Greek bauxite residue (red mud). *Sci. Rep.* **2016**, *6*, 1–13. [[CrossRef](#)] [[PubMed](#)]
53. Reid, S.; Tam, J.; Yang, M.; Azimi, G. Technospheric mining of rare earth elements from bauxite residue (red mud): Process optimization, kinetic investigation, and microwave pretreatment. *Sci. Rep.* **2017**, *7*, 1–9. [[CrossRef](#)] [[PubMed](#)]
54. Davris, P.; Balomenos, E.; Panias, D.; Paspaliaris, I. Selective leaching of rare earth elements from bauxite residue (red mud), using a functionalized hydrophobic ionic liquid. *Hydrometallurgy* **2016**, *164*, 125–135. [[CrossRef](#)]
55. Bolanz, R.M.; Kiefer, S.; Göttlicher, J.; Steininger, R. Hematite (α -Fe₂O₃)—A potential Ce⁴⁺ carrier in red mud. *Sci. Total Environ.* **2018**, 622–623, 849–860. [[CrossRef](#)] [[PubMed](#)]
56. Akcil, A.; Akhmediyeva, N.; Abdulvaliyev, R.; Abhilash; Meshram, P. Overview on extraction and separation of rare earth elements from red mud: Focus on scandium. *Miner. Process. Extr. Metall. Rev.* **2017**, 1–7. [[CrossRef](#)]
57. Yamada, Y. X-ray fluorescence analysis by fusion bead method for ores and rocks. *Rigaku J.* **2010**, *26*, 15–23.
58. Sajó, I.E. X-Ray diffraction quantitative phase analysis of Bayer process solids. In Proceedings of the 10th International Congress of ICSOBA, Bhubaneshwar, India, 28–30 November 2008; pp. 71–76.
59. Sajó, I.E. *XDB Powder Diffraction Phase Analytical System, version 3.107*; Software, Copyright Sajó, I.E. 1987–2016; Sajó, I.E.: Budapest, Hungary, 2005.
60. Menges, F. *Spectragryph-Optical Spectroscopy Software, version 1.0.7*; Universität Konstanz: Obersdorf, Germany, 2017.
61. Lafuente, B.; Downs, R.T.; Yang, H.; Stone, N. The power of databases: The RRUFF project. In *Highlights in Mineralogical Crystallography*; Armbruster, T., Danisi, R.M., Eds.; DE GRUYTER: Berlin, Germany, 2015; pp. 1–30, ISBN 978-3-11-041710-4.
62. Gräfe, M.; Power, G.; Klauber, C. Bauxite residue issues: III. Alkalinity and associated chemistry. *Hydrometallurgy* **2011**, *108*, 60–79. [[CrossRef](#)]
63. Gamaletsos, P.; Godelitsas, A.; Mertzimekis, T.J.; Göttlicher, J.; Steininger, R.; Xanthos, S.; Berndt, J.; Klemme, S.; Kuzmin, A.; Bárdossy, G. Thorium partitioning in Greek industrial bauxite investigated by synchrotron radiation and laser-ablation techniques. *Nucl. Instrum. Methods Phys. Res. Sect. B Beam Interact. Mater. At.* **2011**, *269*, 3067–3073. [[CrossRef](#)]
64. Grice, J.D.; Maisonneuve, V.; Leblanc, M. Natural and synthetic fluoride carbonates. *Chem. Rev.* **2007**, *107*, 114–132. [[CrossRef](#)] [[PubMed](#)]
65. Mouchos, E.; Wall, F.; Williamson, B. High-Ce REE minerals in the Parnassus-Giona bauxite deposits, Greece. *Appl. Earth Sci.* **2017**, *126*, 82–83. [[CrossRef](#)]
66. Gamaletsos, P.N. Mineralogy and Geochemistry of Bauxites from Parnassos-Ghiona Mines and the Impact on the Origin of the Deposits. Ph.D. Thesis, National and Kapodistrian University of Athens, Athens, Greece, 2014.
67. Zaitsev, A.N.; Chakhmouradian, A.R.; Siidra, O.I.; Spratt, J.; Williams, C.T.; Stanley, C.J.; Petrov, S.V.; Britvin, S.N.; Polyakova, E.A. Fluorine-, yttrium- and lanthanide-rich cerianite-(Ce) from carbonatitic rocks of the Kerimasi volcano and surrounding explosion craters, Gregory Rift, northern Tanzania. *Mineral. Mag.* **2011**, *75*, 2813–2822. [[CrossRef](#)]

68. Cui, J.; Hope, G.A. Raman and fluorescence spectroscopy of CeO_2 , Er_2O_3 , Nd_2O_3 , Ti_2O_3 , Yb_2O_3 , La_2O_3 , and Tb_4O_7 . *J. Spectrosc.* **2015**, *2015*, 1–8. [\[CrossRef\]](#)
69. Weber, W.H.; Hass, K.C.; McBride, J.R. Raman study of CeO_2 : Second-order scattering, lattice dynamics, and particle-size effects. *Phys. Rev. B Condens. Matter* **1993**, *48*, 178–185. [\[CrossRef\]](#) [\[PubMed\]](#)
70. Yang, H.; Dembowski, R.F.; Conrad, P.G.; Downs, R.T. Crystal structure and Raman spectrum of hydroxyl-bastnasite-(Ce), $\text{CeCO}_3(\text{OH})$. *Am. Mineral.* **2008**, *93*, 698–701. [\[CrossRef\]](#)
71. De Faria, D.L.A.; Venâncio Silva, S.; Oliveira, M.T. Raman microspectroscopy of some iron oxides and oxyhydroxides. *J. Raman Spectrosc.* **1997**, *28*, 873–878. [\[CrossRef\]](#)
72. Mouchos, E.; Wall, F.; Williamson, B.J.; Palumbo-Roe, B. Easily leachable rare earth element phases in the Parnassus-Giona bauxite deposits, Greece. *Bull. Geol. Soc. Greece* **2016**, *50*, 1952–1958. [\[CrossRef\]](#)
73. Zhuk, Y. Critical Assessment of the Mineralogical Collections at Uppsala University using Raman Spectroscopy. MSc Thesis, Uppsala University, Uppsala, Sweden, 2017.
74. Buzgar, N.; Apopei, A.I. The Raman study of certain carbonates. *Analele Stiintifice Univ. Al. Cuza Din Iasi. Sect. 2 Geol.* **2009**, *55*, 97–112.
75. Miyawaki, R.; Matsubara, S.; Yokoyama, K.; Takeuchi, K.; Terada, Y.; Nakai, I. Kozoite-(Nd), $\text{Nd}(\text{CO}_3)(\text{OH})$, a new mineral in an alkali olivine basalt from Hizen-cho, Saga Prefecture, Japan. *Am. Mineral.* **2000**, *85*, 1076–1081. [\[CrossRef\]](#)
76. Mitchell, R.H.; Welch, M.D.; Chakhmouradian, A.R. Nomenclature of the perovskite supergroup: A hierarchical system of classification based on crystal structure and composition. *Mineral. Mag.* **2017**, *81*, 411–461. [\[CrossRef\]](#)
77. Campbell, L.S.; Henderson, P.; Wall, F.; Nielsen, T.F. Rare earth chemistry of perovskite group minerals from the Gardiner complex, East Greenland. *Mineral. Mag.* **1997**, *61*, 197–212. [\[CrossRef\]](#)
78. Smith, P. Reactions of lime under high temperature Bayer digestion conditions. *Hydrometallurgy* **2017**, *170*, 16–23. [\[CrossRef\]](#)
79. Singh, U.; Mishra, R.S. Simultaneous multielemental analysis of alumina process samples using inductively coupled plasma spectrometry (ICP-AES). *Anal. Chem. Indian J.* **2012**, *11*, 1–5.
80. Teas, E.B.; Kotte, J.J. The effect of impurities on process efficiency and methods for impurity control and removal. In *Proceedings of JBI-JGS Symposium Titled “Bauxite/Alumina Industry in the Americas”*; Geological Society of Jamaica: Kingston, Jamaica, 1980; Volume 23, pp. 100–129.
81. Brookins, D.G. *Eh-pH Diagrams for Geochemistry*; Springer Science & Business Media: Berlin, Germany, 1988; ISBN 978-3-642-73093-1.
82. Brookins, D.G. Eh-pH diagrams for the rare earth elements at 25 C and one bar pressure. *Geochem. J.* **1983**, *17*, 223–229. [\[CrossRef\]](#)
83. Bánvölgyi, G.; Toth, A.C.; Tassy, I. In situ formation of sodium aluminum hydrosilicate from kaolinite. *Light Met.* **1991**, *1*, 5–15.
84. Nickel, E.H.; McAdam, R.C. Niobian perovskite from Oka, Quebec; A new classification for minerals of the perovskite group. *Can. Mineral.* **1963**, *7*, 683–697.
85. Mitchell, R. Perovskites: A revised classification scheme for an important rare earth element host in alkaline rocks. In *Rare Earth Minerals. Chemistry, Origin and Ore Deposits*; Jones, A.P., Wall, F., Williams, C.T.W., Eds.; Mineralogical Society Series; Chapman and Hall: London, UK, 1996; Volume 7, pp. 41–76.
86. Atta, N.F.; Galal, A.; El-Ads, E.H. Perovskite nanomaterials—synthesis, characterization, and applications. In *Perovskite Materials—Synthesis, Characterisation, Properties, and Applications*; Pan, L., Ed.; InTech: London, UK, 2016; pp. 107–151. [\[CrossRef\]](#)
87. Castor, S.B.; Hedrick, J.B. Rare earth elements. In *Industrial Minerals & Rocks: Commodities, Markets, and Uses*; Kogel, J.E., Trivedi, N.C., Barker, J.M., Krukowski, S.T., Eds.; Society for Mining, Metallurgy, and Exploration: Littleton, CO, USA, 2006; pp. 769–779, ISBN 978-0-87335-233-8.
88. Thirumalairajan, S.; Girija, K.; Hebalkar, N.Y.; Mangalaraj, D.; Viswanathan, C.; Ponpandian, N. Shape evolution of perovskite LaFeO_3 nanostructures: A systematic investigation of growth mechanism, properties and morphology dependent photocatalytic activities. *RSC Adv.* **2013**, *3*, 7549–7561. [\[CrossRef\]](#)
89. Feng, D.; Maram, P.S.; Mielewczyk-Gryn, A.; Navrotsky, A. Thermochemistry of rare earth perovskites $\text{Na}_{3x}\text{RE}_{0.67-x}\text{TiO}_3$ (RE = La, Ce). *Am. Mineral.* **2016**, *101*, 1125–1128. [\[CrossRef\]](#)

90. Manceau, A.; Gorshkov, A.I.; Drits, V.A. Structural chemistry of Mn, Fe, Co, and Ni in manganese hydrous oxides: Part II. Information from EXAFS spectroscopy and electron and X-ray diffraction. *Am. Mineral.* **1992**, *77*, 1144–1157.
91. Eliopoulos, D.; Economou, G.; Tzifas, I.; Papatrechas, C. The potential of rare earth elements in Greece. In Proceedings of the 1st International Conference on European Rare Earth Resources, Heliotos Conferences Ltd., Milos, Greece, 4–7 September 2014; pp. 308–316.
92. Pourret, O.; Davranche, M. Rare earth element sorption onto hydrous manganese oxide: A modeling study. *J. Colloid Interface Sci.* **2013**, *395*, 18–23. [[CrossRef](#)] [[PubMed](#)]
93. Dubinin, A.V. Geochemistry of Rare Earth Elements in the Ocean. *Lithol. Miner. Resour.* **2004**, *39*, 289–307. [[CrossRef](#)]
94. Astakhova, N.V.; Sattarova, V.V. The REE species and their distribution in ferromanganese crusts in the Sea of Japan. *Russ. Geol. Geophys.* **2012**, *53*, 649–656. [[CrossRef](#)]
95. Aiglsperger, T.; Proenza, J.A.; Lewis, J.F.; Labrador, M.; Svojtka, M.; Rojas-Puron, A.; Longo, F.; Ďurišová, J. Critical metals (REE, Sc, PGE) in Ni laterites from Cuba and the Dominican Republic. *Ore Geol. Rev.* **2016**, *73*, 127–147. [[CrossRef](#)]
96. Jordens, A.; Cheng, Y.P.; Waters, K.E. A review of the beneficiation of rare earth element bearing minerals. *Miner. Eng.* **2013**, *41*, 97–114. [[CrossRef](#)]
97. Goronovski, A.; Joyce, P.J.; Björklund, A.; Finnveden, G.; Tkaczyk, A.H. Impact assessment of enhanced exposure from Naturally Occurring Radioactive Materials (NORM) within LCA. *J. Clean. Prod.* **2018**, *172*, 2824–2839. [[CrossRef](#)]
98. Nuccetelli, C.; Pontikes, Y.; Leonardi, F.; Trevisi, R. New perspectives and issues arising from the introduction of (NORM) residues in building materials: A critical assessment on the radiological behaviour. *Constr. Build. Mater.* **2015**, *82*, 323–331. [[CrossRef](#)]



© 2018 by the authors. Licensee MDPI, Basel, Switzerland. This article is an open access article distributed under the terms and conditions of the Creative Commons Attribution (CC BY) license (<http://creativecommons.org/licenses/by/4.0/>).